Research Article

TRANSPARENT PROCESS SOURCE DATA OPEN ACCESS

Life Science Alliance

The CDKL5 kinase undergoes liquid–liquid phase separation driven by a serine-rich C-terminal region

Stefania Boggio Bozzo[1,*], Marco Dell'Oca[1,*], Serena Vaglietti[1], Antonia Gurgone[1], Vita Cardinale[1], Gregorio Ragazzini[2,3], Andrea Alessandrini[2,3], Luca Colnaghi[4], J Fernando Bazan[5], Mirella Ghirardi[1], Maurizio Giustetto[1], Ferdinando Fiumara[1]

The *CDKL5* gene encodes a protein kinase involved in nervous system development and function. Pathogenic variants in this gene can cause a severe neurodevelopmental CDKL5 deficiency disorder (CDD). The CDKL5 protein contains a catalytic N-terminal domain (NTD) and a less characterized C-terminal domain (CTD). We discovered that the CTD is a serine-rich low-complexity region driving liquid–liquid phase separation (LLPS), a biophysical process controlling protein localization and function, by which CDKL5 forms intracellular membraneless condensates. A CTD internal fragment (CTIF) plays a pivotal LLPS-promoting role, along with the distal portion of the protein. In CDD, transcripts carrying pathogenic nonsense or frameshift mutations introducing distal premature termination codons may escape nonsense-mediated decay, producing CDKL5 proteins with a variably truncated CTD. We found that two distal truncations, removing part of the CTIF and the downstream protein tail, significantly reduce CDKL5 LLPS and catalytic function. These findings demonstrate that CDKL5 undergoes LLPS, driven by a CTD region whose loss in distally truncated forms of the protein—by impairing LLPS and functional activity—may play a role in the molecular pathogenesis of CDD.

DOI 10.26508/lsa.202503402 | Received 26 May 2025 | Revised 13 February 2026 | Accepted 19 February 2026 | Published online 10 March 2026

Introduction

The *cyclin-dependent kinase-like 5* (CDKL5) is a serine–threonine protein kinase whose activity has been linked to the regulation of a variety of cellular processes ranging from DNA repair to synapse assembly and function in neurons (La Montanara et al, 2015; Pizzo et al, 2016, 2020; Canning et al, 2018; Khanam et al, 2021; Gurgone et al, 2023). However, only relatively few of its direct protein targets and mechanisms of action have been identified (Katayama et al, 2020; Van Bergen et al, 2022; Silvestre et al, 2024). Different isoforms of the CDKL5 kinase are generated by alternative splicing, displaying tissue-specific expression patterns, one of which is highly expressed in the nervous system (Hector et al, 2016; Frasca et al, 2022). The domain architecture of the protein consists of an N-terminal domain (NTD) with catalytic function followed by a long C-terminal domain (CTD). Although the structure and function of the catalytic domain are quite well characterized (Canning et al, 2018), those of the CTD remain largely elusive. The CTD, which bears two nuclear localization signals (NLSs) and a nuclear export signal (NES), is thought to regulate the subcellular localization and catalytic activity of CDKL5 (Bertani et al, 2006; Rusconi et al, 2008; Frasca et al, 2022).

Mutations in the *CDKL5* gene can cause the CDKL5 deficiency disorder (CDD), a neurodevelopmental epileptic encephalopathy characterized by early-onset seizures, severe neurocognitive impairment, and sensorimotor alterations, which was originally classified as a Rett syndrome variant (Leonard et al, 2022). Moreover, *CDKL5* mutations can also lead to related neurodevelopmental conditions like West syndrome, also characterized by epileptic encephalopathy (Kato, 2006).

Most CDD-related missense mutations affect the NTD and can impair or abolish its kinase domain function (Canning et al, 2018). Remarkably, however, numerous CDD-related nonsense and frameshift mutations, some of which may lead to the production of truncated variants of the protein, occur not only in the gene exons encoding the kinase domain but also in those encoding the CTD (Fehr et al, 2015; Leonard et al, 2022). These mutations introduce premature stop codons (PTCs) in CDKL5 transcripts, which may then undergo a process of nonsense-mediated decay (NMD) that prevents their translation into protein. However, evidence exists that transcripts bearing PTCs beyond codon 693 may escape NMD leading to the production of distally truncated forms of CDKL5 (Bahi-Buisson et al, 2008; Feng et al, 2025), especially in neurons, cells in which NMD efficiency is known to be lower (Palou-Márquez & Supek, 2025). These truncated forms of the protein bear an intact catalytic kinase domain and a variably shortened CTD. These

[1]Rita Levi-Montalcini Department of Neuroscience, University of Turin, Turin, Italy [2]Department of Physics, Informatics and Mathematics, University of Modena, Modena, Italy [3]CNR Nanoscience Institute, Modena, Italy [4]Division of Neuroscience, IRCCS San Raffaele Scientific Institute, Milan, Italy [5]h Bioconsulting LLC, Stillwater, MN, USA

Correspondence: maurizio.giustetto@unito.it; ferdinando.fiumara@unito.it
*Stefania Boggio Bozzo and Marco Dell'Oca contributed equally to this work

findings indicate that the integrity of the kinase domain alone may not be sufficient to prevent CDD, highlighting the importance of the CTD in ensuring the proper physiological function of the CDKL5 protein.

The clinical spectrum of CDKL5-related disorders is quite heterogeneous, with limited genotype–phenotype correlations linking specific mutations to defined clinical outcomes (Fehr et al, 2015; Demarest et al, 2019; Leonard et al, 2022). Thus, a detailed understanding of the molecular and functional features of the CDKL5 CTD may provide key knowledge to better understand both the physiological roles of this conspicuous protein domain, which comprises about two thirds of the protein length, and the pathological impact of those CDD-related truncating mutations that variably shorten its length.

To address these issues, we performed a systematic in silico analysis of the compositional features and evolutionary dynamics of CDKL5. This analysis revealed that the CTD is a low-complexity region (LCR) of the protein highly enriched in serine residues and with a high predicted propensity to undergo liquid–liquid phase separation (LLPS), a biophysical process of condensation controlling protein localization and function (Alberti & Dormann, 2019). We found that CDKL5 is indeed able to form LLPS-driven condensates in neuronal and nonneuronal cells, as revealed by morphological, molecular dynamics, and biochemical criteria. Through a molecular dissection approach, we found that CDKL5 LLPS relies on the interplay between the CTD and the NTD, and that it is promoted particularly by a serine-rich CTD internal fragment (CTIF) together with the more distal portion of the protein. Distally truncated forms of CDKL5 lacking these C-terminal parts of the protein (CDKL5-S726X and CDKL5-R781X), such as those that can be produced in CDD from transcripts escaping NMD, display both altered LLPS behavior, which directly impacts subcellular localization, and reduced catalytic activity. These findings have important implications for our understanding of CDKL5 physiological function and suggest that aberrant LLPS may play a role in the molecular pathogenesis of CDD forms caused by mutations leading to distal truncations of the protein.

Results

The CDKL5 CTD is highly enriched in serine residues

To gain a deeper understanding of the possible biological roles of the CDKL5 CTD, we undertook a systematic in silico analysis of its compositional and structural features in comparison with those of the whole CDKL5 protein, its NTD, and the entire human proteome (Figs 1 and S1).

We first analyzed the occurrence and distribution of the 20 amino acids in CDKL5 (the 960-residue isoform enriched in the brain, or $CDKL5_{107}$; Frasca et al, 2022) and its two major domains, that is, the NTD (a.a. 1–297), mostly occupied by the catalytic kinase domain (a.a. 13–297), and the downstream CTD (a.a. 298–960). Moreover, we quantified the mean occurrence of the 20 amino acids across all proteins in the UniProt reference human proteome to identify over- and under-represented residues in CDKL5 and its two major domains (Figs 1A–C and S1A and C).

This analysis revealed that serine is the most represented amino acid, both in CDKL5 in toto (13.56%) and in its CTD (17.67%), largely exceeding (+68% and +119%, respectively) the mean percent occurrence of this residue in the human proteome (8.03%; Figs 1A and B and S1A and B). Consistent with these observations, the CAST algorithm identified the CTD as a low-complexity region within CDKL5 (Fig 1A). Notably, serine is much less represented in the catalytic NTD (4.39%, i.e., −45.35% versus proteome). Leucine (L) is the most abundant amino acid (13.51%) in the NTD, together with the charged amino acids glutamate (E; 9.8%) and lysine (K; 8.11%; Figs 1A and B and S1A and B). When we analyzed the distribution of serine and leucine in CDKL5 (Figs 1A and S1A), we observed that serine residues are predominantly located in the CTD, scattered along its entire length, also in doublets or triplets. Leucine residues are more abundant in the NTD, especially near the junction with the CTD, whereas the frequency of charged residues peaks in the initial portion of the NTD (Figs 1A and S1A).

The amino acid composition of the CTD appears to deviate substantially from the average composition of human proteins. Indeed, the CTD is enriched in polar (S, N, T, Q), positively charged (K, R, H), and proline (P) residues, and depleted of hydrophobic and negatively charged ones (Figs 1B and S1B).

These differential amino acid distributions across the two domains appear to mark structurally distinct regions of the protein. Indeed, as visible in an AlphaFold structural model of CDKL5 (Fig 1C), the serine-rich portion of the protein is predicted to form long random coil loops surrounding the central catalytic core like a shell. While lacking experimental validation, such prediction of a disordered organization of the CTD is consistent with that of conventional structural prediction tools, such as IUPred3 (Erdős et al, 2021; Fig S1C). Leucine residues, in contrast, are concentrated within the α-helices of the kinase domain in the NTD, consistent with the experimentally determined structure reported in the PDB database (PDB ID: 4bgq; Canning et al, 2018; Fig S1D).

Such a serine-rich CTD is either absent or considerably shorter in the other four members of the human CDKL family of kinases (CDKL1-4), which display a high degree of sequence similarity to CDKL5 in the NTD (Fig 1D). The amino acid composition of the five members of the CDKL family reflects this fact. Indeed, the occurrence of serine residues in CDKL1-4 is similar to that found in the whole proteome (8.03%), or even lower (4.2% in CDKL1, 6.28% in CDKL2, 7.09% in CDKL3, 5.54% in CDKL4), in stark contrast to what is observed in CDKL5 (13.54%; Fig 1E). Interestingly, short portions of the CDKL2 and CDKL3 CTDs display a local concentration of serine residues (Fig 1E).

Overall, these findings indicate that the human CDKL5 CTD is a long LCR, highly enriched in serine residues, that is unique to CDKL5 among the CDKL paralogs.

The serine richness of the CTD is phylogenetically conserved in vertebrates and peaks in mammals

To determine whether the observed enrichment in serine residues of the CDKL5 CTD is a human-specific or a phylogenetically conserved feature of the protein, we systematically analyzed the

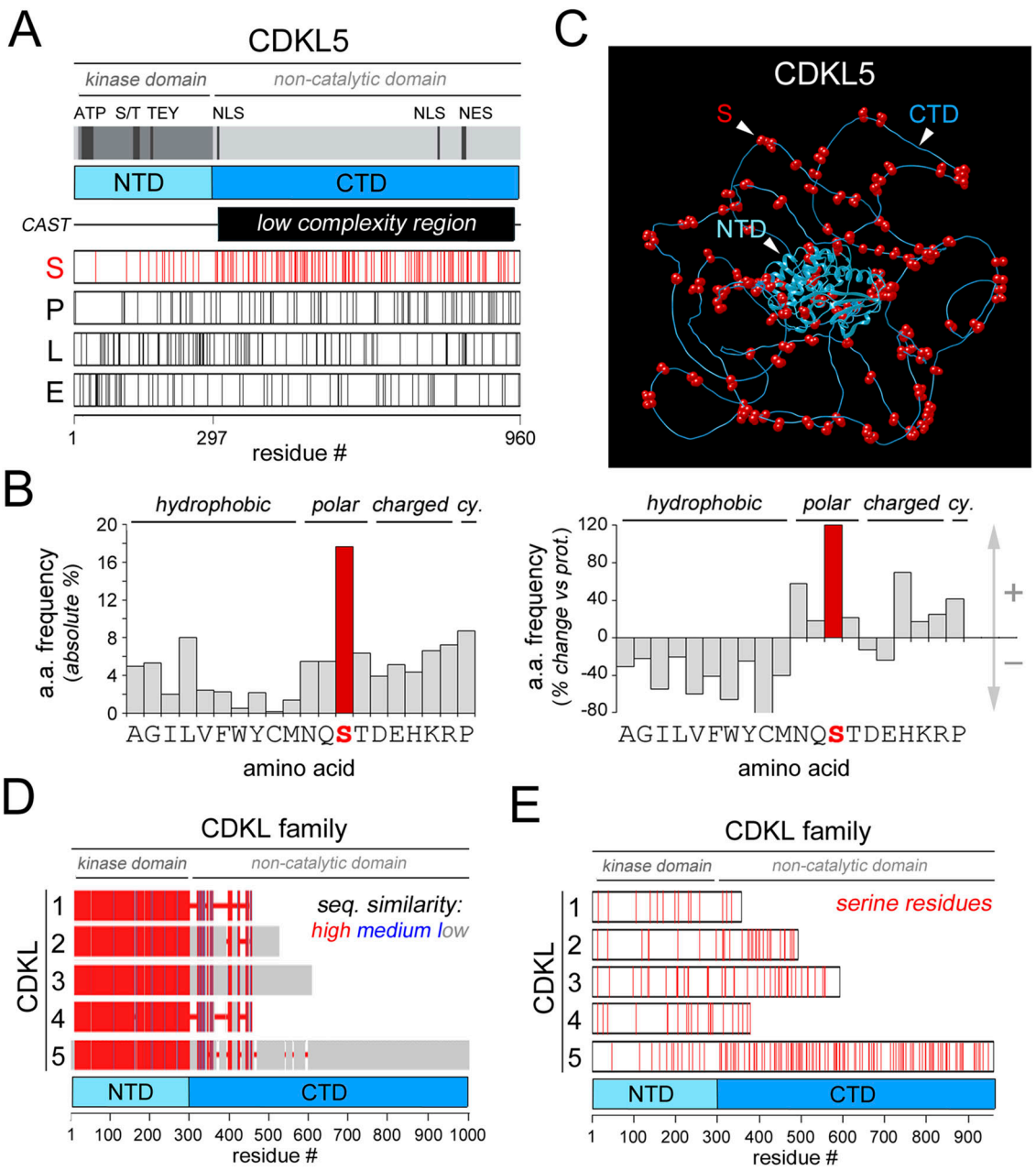

Figure 1. CDKL5 C-terminal domain (CTD) is highly enriched in serine residues.
(A) The *gray bar* is a schematic representation of the CDKL5 protein highlighting the kinase domain (*dark gray*) and, in *black*, notable functional sites, that is, the ATP-binding site (ATP), the catalytic site (S/T), and the activation loop site (TEY), two nuclear localization signals (NLSs), and a nuclear export signal (NES). The *colored bar* highlights the NTD (*cyan*), containing the kinase domain, and the C-terminal domain (CTD, *turquoise*) formed by a low-complexity region, as identified by the CAST algorithm (*black bar*). *Thin vertical lines* in the four white bars below indicate the position of the indicated amino acid residues (S in *red*; P, L, and E in *black*). **(B)** The bar graph on the *left* plots the percent occurrence of the 20 amino acids within the CDKL5 CTD. Note the high percentage of serine residues (*red bar*). The bar graph on the *right* plots the difference between the percent occurrence of the 20 amino acids in the CTD and their mean percent occurrence across all proteins of the human proteome. This difference reaches the highest value (~120%) for serine residues. **(C)** AlphaFold structural model of human CDKL5. The N-terminal domain (*cyan*), the CTD (*turquoise*), and serine residues (*red spheres*) are highlighted. The CTD displays a mostly random coil conformation, forming a shell around the central catalytic domain, and is highly enriched in serine residues. **(D)** Schematic representation of an alignment of the primary sequences of human CDKL1-5 obtained using Cobalt (NCBI). *Red*, *blue*, and *gray* bars indicate, respectively, high, intermediate, and low degrees of sequence similarity along the primary sequence alignment. **(E)** Schematic representation of CDKL1-5 (*white bars*) in which the position of serine residues is highlighted in *red*. Note how CDKL5 has the longest serine-rich CTD.
Source data are available for this figure.

primary sequence composition of CDKL5 orthologs from 332 species belonging to major clades/taxa of different stem ages along the vertebrate lineage (Fig 2A; Table S1). We found that the frequency of serine residues in the CTD is higher than that found in the NTD even in species belonging to clades/taxa with the oldest stem age, such as Agnatha (10.69% in *Petromyzon marinus*), with a

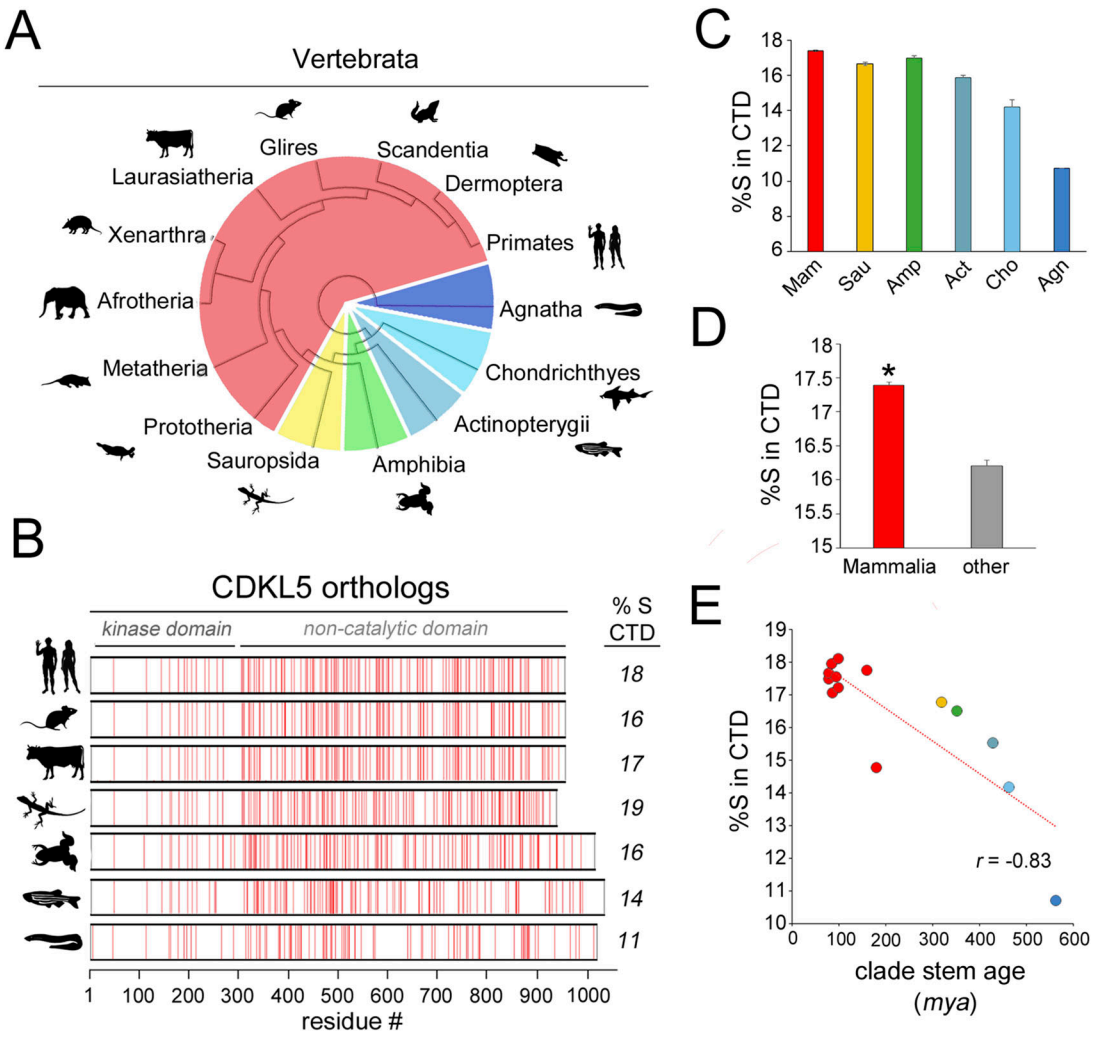

Figure 2. Evolutionary trends in the serine enrichment of the CDKL5 C-terminal domain (CTD) in vertebrates.
(A) Phylogenetic tree encompassing some of the main clades/taxa of the vertebrate lineage. Mammalia, Sauropsida, Amphibia, Actinopterygii, Chondrichthyes, and Agnatha are highlighted, respectively, in *red*, *yellow*, *green*, *teal*, *cyan*, and *blue*. **(B)** Schematic representation of CDKL5 orthologs (*white bars*) of seven vertebrate species from representative vertebrate clades/taxa in which the position of serine residues is highlighted in *red*. The black silhouettes indicate, from *top* to *bottom*, *Homo sapiens*, *Mus musculus*, *Bos taurus*, *Anolis carolinensis*, *Xenopus laevis*, *Danio rerio*, and *Petromyzon marinus*. The enrichment in serine residues increases going from species belonging to clades/taxa with older stem ages to species belonging to younger clades along the vertebrate lineage. **(C)** Bar graph showing the mean percent occurrence of serine residues in the CTD of CDKL5 orthologs of the indicated clades/taxa (Mammalia, *Mam*, n = 133; Sauropsida, *Sau*, n = 108; Amphibia, *Amp*, n = 9; Actinopterygii, *Act*, n = 79; Chondrichthyes, *Cho*, n = 2; and Agnatha, *Agn*, n = 1). Note the increase in serine occurrence going from Agnatha to Mammalia. **(D)** Bar graph displaying the mean percent occurrence of serine residues in the CTD of CDKL5 orthologs from mammalian (*red*) versus nonmammalian species (*other*, *gray*). **(E)** Scatterplot displaying the significant correlation between clade/taxa divergence times and the mean percent occurrence of serine residues in the CTD (n = 14 clades/taxa, as listed in (A)).
Source data are available for this figure.

progressive increase in younger clades, reaching its maximum level in mammals (17.39% on average; Fig 2B–E). Overall, the mean percent occurrence of serine residues in the CTD is significantly higher in mammalian than in nonmammalian species (17.39 ± 0.04, n = 133 species, versus 16.20 ± 0.08, n = 199, $P < 0.001$, *t* test; Fig 2D). Moreover, the increase in serine occurrence in the CTD correlates significantly with clade/taxa stem age along the vertebrate lineage ($r = -0.83$, n = 14, $P < 0.001$; Fig 2E).

Taken together, these findings indicate that the enrichment in serine residues is a phylogenetically ancient feature of CDKL5 that has been preserved and even enhanced in younger clades along the vertebrate lineage, strongly suggesting functional relevance.

CDKL genes have also been identified in invertebrates, such as *Caenorhabditis elegans* and *Drosophila melanogaster*. These species possess only a single *CDKL* gene, more closely related to the vertebrate CDKL1-4 group, bearing a relatively short CTD. Interestingly, the CTDs of both these two invertebrate CDKLs contain LCRs enriched in either alanine/glutamine (A/Q in *D. melanogaster*) or asparagine/serine (N/S in *C. elegans*), with an overall configuration similar to that of human CDKL4 (Fig S2). These observations suggest the possibility that LCRs may have appeared

multiple times in *CDKL* genes through convergent molecular evolution (see the Discussion section).

The serine-rich CTD is predicted to undergo LLPS

As serine-rich LCRs are candidate mediators of protein oligo-/polymerization and phase separation (Lilliu et al, 2018; Sabari et al, 2018; Peng et al, 2026), we sought to determine whether the CTD may promote CDKL5 LLPS. The FuzDrop algorithm (Hardenberg et al, 2020) predicted a high overall probability for the protein to undergo LLPS (*probability of spontaneous liquid–liquid phase separation* [pLLPS] > 0.99 on a 0-to-1 scale). Strikingly, most of the residues in the serine-rich CTD, unlike those in the kinase domain, displayed above-threshold per-residue P_{DP} scores (≥0.6, on a 0–1 scale with a positive prediction threshold of 0.6; Fig 3A). In the FuzDrop prediction profile, it was possible to identify three major uninterrupted peaks (*1*, *2*, and *3* in Fig 3A) with high P_{DP} scores (>0.8). Shorter LLPS-prone regions were identified at the ends of the CTD (*white squares*) and within the NTD (*black asterisks*). Such a distinctly bipartite distribution of low and high scores across the two CDKL5 domains was also clearly visible when per-residue P_{DP} scores were visualized in pseudocolors on the AlphaFold structural model of CDKL5 (Fig 3B).

A similar analysis was performed for the other members of the CDKL family. CDKL1-4 all displayed low pLLPS scores, consistent with their shorter CTDs (Fig S3A and B). Indeed, the overall FuzDrop LLPS probability score is much lower for CDKL2 (0.33) and CDKL3 (0.59) than for CDKL5 (0.99). The same score is extremely low for CDKL1 (0.11) and CDKL4 (0.14), which have very short C-terminal tails (Fig 1D and E). Notably, these scores correlated with the density of serine residues in the CTDs of the five kinases ($r = 0.95$, $n = 5$, $P < 0.02$; Fig S3B). However, some regions of the CTD of CDKL2, CDKL4, and especially CDKL3 displayed above-threshold per-residue P_{DP} scores suggesting the possibility that they may have some degree of LLPS propensity. Interestingly, also the N/S-rich and A/Q-rich tails of the CDKL kinases in *C. elegans* and *D. melanogaster*, respectively, display above-threshold P_{DP} scores (Fig S2). This observation further supports the notion that compositionally distinct, but similarly LLPS-prone, LCRs may have evolved in a convergent manner across clades (Vaglietti et al, 2023).

Taken together, these findings identify the long serine-rich LCR of CDKL5 as a likely candidate mediator of LLPS. The AlphaFold structural model also suggests that this CDKL5 region may form an allosteric shell (Taylor et al, 2022) regulating the catalytic activity of the protein and mediating its homo- and heterotypic protein–protein interactions, including those driving LLPS.

CDKL5 forms intracellular LLPS-driven condensates in neuronal and nonneuronal cells

To determine whether CDKL5 undergoes LLPS in the cellular context, we tested in different cell types whether the protein forms rounded, membraneless foci ("condensates"), as typical of LLPS-prone proteins, and whether these foci display distinctive properties of LLPS-driven protein assemblies.

By means of immunocytochemistry and Airyscan super-resolution confocal microscopy, we analyzed the subcellular distribution of CDKL5 in cultured neuronal (primary hippocampal neurons and differentiated NG108-15 cells) and nonneuronal (HEK293) cells using a monoclonal antibody (Fig 3C–F). We found that endogenous CDKL5 forms rounded foci both in the nucleus and in the cytoplasm of all these cell types. In neuronal cells, the foci were also present in the axonal and dendritic compartments. The relative proportion of intra- versus extranuclear condensates varied with the cell type. In primary neurons (Fig 3C) and differentiated NG108-15 cells (Fig 3D and E), condensates were prevalently distributed in the cytoplasm, the axon, and the dendritic tree. In HEK293 cells, they were more concentrated in nuclei, although they were also present in the cytoplasm (Fig 3F). These findings are consistent with previous observations of cell type–specific subcellular distribution and nucleocytoplasmic shuttling of the protein (Lin et al, 2005; Rusconi et al, 2008; Oi et al, 2017). In primary hippocampal neurons, the dendritic CDKL5 condensates colocalized, or were in close juxtaposition, with clusters of the presynaptic marker protein synaptophysin, in agreement with the fact that CDKL5 is present in both pre- and postsynaptic compartments (Fig 3C). Presynaptic varicosities formed by NG108-15 cells (Han et al, 1991; Fig 3D, *right panel*, and Fig 3E) were particularly enriched in CDKL5 condensates.

Control neuronal cell cultures from CDKL5 knockout (KO) mice (Fig S4A and B) immunostained with the same antibody displayed some nonspecific staining in the form of faint patches and much rarer puncta in the cell body (mostly perinuclear) and neurites, in stark contrast to the high number of bright foci observed in the same compartments in WT neurons. These findings indicate that despite some background staining, the antibody is sufficiently specific for CDKL5 to conclude that the vast majority of the puncta observed in cells after immunocytochemistry are indeed CDKL5 condensates. This conclusion is further corroborated by the fact that the exogenously expressed CDKL5-GFP protein displays a condensation pattern (Fig 4A–C) similar to that of the endogenous protein as revealed by immunocytochemistry. The CDKL5-GFP foci increased in size, also by coalescence, in a time- and expression level–dependent manner, as generally observed for LLPS-driven condensates (Rebane et al, 2020; *see also below*). Such coalescence was more pronounced in HEK293 cells (Fig 4C) than in differentiated neuronal NG108-15 cells (Fig 4A). In these neuronal cells, the condensates remained generally smaller and more distributed throughout the neuritic tree, matching the distribution pattern of endogenous CDKL5. In either cell type, both endogenous and exogenously expressed CDKL5 displayed variable distribution patterns and degrees of condensation across cells, likely related to cell cycle phases in mitotic HEK293 cells (Barbiero et al, 2017) or differentiation stages in neuronal NG108-15 cells.

These findings provide morphological evidence that both endogenous and exogenously expressed CDKL5 form discrete, rounded intracellular foci as typical of proteins undergoing LLPS (Shin et al, 2017; Vaglietti et al, 2023).

To assess whether the CDKL5 intracellular foci are membraneless structures, as typical of LLPS-driven condensates, we performed *correlative light and electron microscopy* (CLEM) ultrastructural analyses of cells expressing CDKL5-GFP. CLEM scans, both in the nucleus (Fig 4D) and in the cytoplasm (Fig 4E),

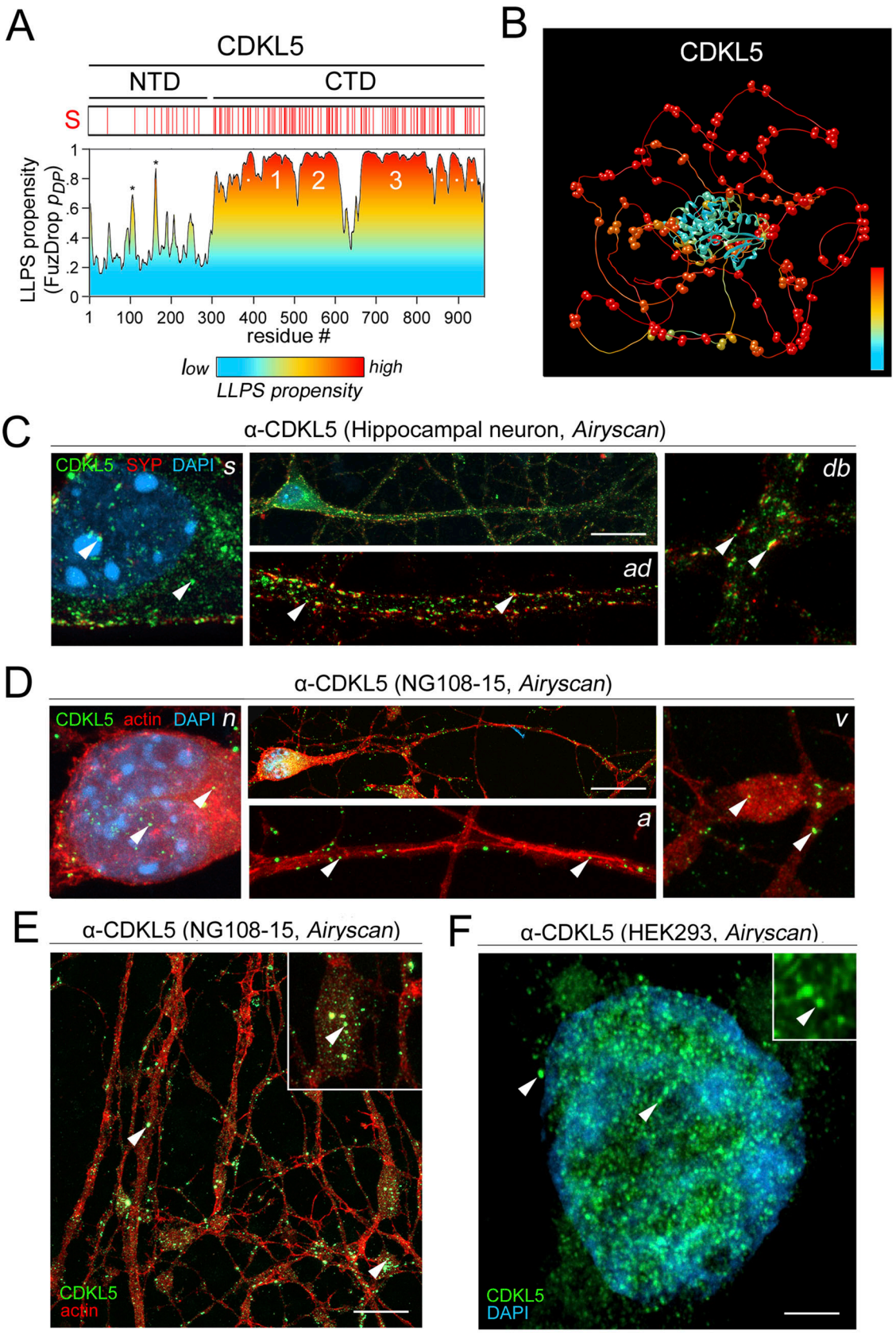
A
CDKL5
NTD
CTD
S
LLPS propensity (FuzDrop p_{DP})
1
2
3
residue #
low
high
LLPS propensity
B
CDKL5
C
α-CDKL5 (Hippocampal neuron, Airyscan)
CDKL5 SYP DAPI
s
ad
db
D
α-CDKL5 (NG108-15, Airyscan)
CDKL5 actin DAPI
n
a
v
E
α-CDKL5 (NG108-15, Airyscan)
CDKL5
actin
F
α-CDKL5 (HEK293, Airyscan)
CDKL5
DAPI

show that CDKL5 foci are not delimited by membranes. Some foci were found in small clusters, and some of them appeared to be in the process of coalescing with each other (Fig 4E, *right panel*), a hallmark feature of LLPS-driven condensates (Vaglietti et al, 2023). Moreover, some large foci appeared to be hollow (Fig 4D, *right panel*), displaying an internal cavity visible in both confocal fluorescence images and electron microscopy scans. In principle, these condensates may represent either donut-like toroidal structures or hollow spheres. Their inner cavity appeared to be quite central within condensates and we did not observe highly eccentric holes, which would be expected for toroidal structures not parallel to the sectioning and observation plane. Moreover, we did not observe linearly elongated condensate-like structures, which would be expected for toroids seen laterally. These two observations suggest that the larger condensates may be hollow spherical structures. Interestingly, morphologically similar structures have been recurrently observed for other LLPS-prone proteins, such as TDP-43 and Oskar. This configuration of the condensates derives from their internal partitioning related to local changes in the physicochemical environment or to the presence of coseparated molecular components, such as other proteins and/or nucleic acids (Schmidt & Rohatgi, 2016; Kistler et al, 2018; Dai & Yang, 2024), which may be present in the inner part of the condensates.

Finally, we tested whether, in addition to their morphology and ultrastructure, the intracellular CDKL5 foci display additional hallmark features of LLPS-driven protein condensates (Sabari et al, 2018; Basu et al, 2020).

We first tested the dynamics of CDKL5 molecular diffusion between the condensates and the surrounding cellular environment by measuring *fluorescence recovery after photobleaching* (FRAP; Fig 5A). These experiments revealed rapid FRAP within 60 s, which could be fitted to an exponential curve with a recovery half-time ($t_{1/2}$) of 12.2 s and a mobile fraction of 74% (mean values of n = 11 condensates), indicative of rapid molecular exchange between the foci and the surrounding environment, in the range of other LLPS-prone proteins (e.g., Shin et al, 2017; Fan et al, 2020; Vaglietti et al, 2023).

Second, in live-cell imaging experiments, we observed that smaller CDKL5-GFP condensates tend to coalesce into larger ones in a time-dependent manner, another typical feature of LLPS-driven, liquid-like condensates (Fig 5B; Video 1).

Third, we tested whether the CDKL5 foci are sensitive to 1,6-hexanediol (1,6-Hex; Fig 5C), a compound known to disrupt the relatively weak intermolecular interactions underlying LLPS (Ulianov et al, 2021; Vaglietti et al, 2023). Toward this aim, we compared the condensation of endogenous CDKL5 in NG108-15 cells either treated with 1,6-Hex (for 5 or 15 min) or mock-treated with only the vehicle (DMEM), and then immunostained to detect CDKL5. We found that 1,6-Hex caused an overall significant reduction in the fraction of immunostained cell area occupied by condensates ($F_{(2,44)}$ = 11.78, P < 0.001, one-way ANOVA) and in the number of condensates per AF488-positive unit area ($F_{(2,44)}$ = 12.28, P < 0.001, one-way ANOVA; Fig 5D). Indeed, already at 5 min, the area occupied by condensates was reduced to 39.92% ± 9.86% (n = 15 microscopy fields) of that measured under control conditions (100% ± 15.45%, n = 19, P < 0.01, Newman–Keuls [NK] post hoc test; data normalized to the control group mean). This reduction was even more pronounced at 15 min (18.83% ± 6.59%; n = 13, P < 0.01, NK post hoc test versus control group). Similarly, the number of condensates was reduced to 42.15% ± 3.11% (n = 15 microscopy fields) and 18.37% ± 3.58% (n = 13), respectively, after 5 and 15 min of 1,6-Hex treatment, of the number measured in the control condition (100% ± 2.45%, n = 19 nuclei, P < 0.001, NK post hoc test; data normalized to the control group mean; Fig 5D).

A similar sensitivity to 1,6-Hex was also observed for condensates formed by exogenously expressed CDKL5-GFP in HEK293 cells (Fig 5E). Indeed, 1,6-Hex application for 15 min induced a ∽86% reduction of the area occupied by condensates in comparison with control conditions (100% ± 4.74%, n = 64 fields, versus 13.97% ± 2.35%, n = 47, respectively, P < 0.001, t test; Fig 5F). A similar effect was observed for the number of condensates per GFP-positive unit area (100% ± 4.30%, n = 64 microscopy fields, versus 14.91% ± 2.11%, n = 47, respectively, P < 0.001, t test; Fig 5F).

Taken together, these findings indicate that intracellular CDKL5 foci display morphological, ultrastructural, dynamic, and biochemical hallmark features of LLPS-driven condensates.

The serine-rich CTD has a prominent role in mediating CDKL5 LLPS

To experimentally determine which portion of the CDKL5 protein may drive LLPS, we started by comparing the relative ability to

Figure 3. Endogenous CDKL5 forms condensate-like foci in neuronal and nonneuronal cells.
(A) The *lower graph* plots the per-residue FuzDrop LLPS propensity score (P_{DP} score) along the CDKL5 primary sequence. The area under the curve is colored using a *blue-to-red gradient* to highlight the protein regions with the highest LLPS propensity (P_{DP} score > 0.6; *orange*/*red*). The *white bar* above represents the protein with serine residues highlighted in *red*. The serine-rich C-terminal domain contains three extended regions with high LLPS propensity (1–3) and minor peaks marked by *white dots*. A few high-propensity peaks are also present within the N-terminal domain (*asterisks*). **(A, B)** AlphaFold structural model of human CDKL5, as in Fig 1C, pseudo-colored to display the FuzDrop per-residue LLPS propensity score using the same color scale as in panel (A). The random coil serine-rich C-terminal domain, surrounding the central catalytic domain, is the region with the highest scores (*orange*/*red*). **(C)** *Central upper panel*. Super-resolution (Airyscan) confocal fluorescence micrograph of a mouse primary hippocampal neuron immunostained to detect endogenous CDKL5 (*green*) and the presynaptic marker synaptophysin 1 (SYP, *red*). The nucleus was stained using DAPI (*blue*). The *left*, *lower middle*, and *right panels* show, respectively, magnified details of the neuronal somatic compartment (s), the proximal part of the apical dendrite (*ad*), and a more distal dendritic branch (*db*). Both intra- and extranuclear condensate-like foci (*arrowheads*) are visible. Scale bar: 20 μm. **(D)** As in (C) for a differentiated NG108-15 neuronal cell. The *red* staining, obtained using fluorescently labeled phalloidin, marks actin. The *middle lower panel* shows a detail of the axon (*a*), and the *right panel* displays a neuritic varicosity (*v*). *Arrowheads* highlight condensate-like foci. Scale bar: 20 μm. **(E)** Neuropil formed by intermeshed neurites, with varicosities, of differentiated NG108-15 cells. Note the enrichment of CDKL5 foci in varicosities. The *inset* in the *upper right corner* shows a magnified detail of the image encompassing a varicosity. The *arrowhead* indicates one of the condensate-like foci. Scale bar: 10 μm. **(F)** CDKL5 immunostaining (*green*) in a HEK293 cell. DAPI (*blue*) marks the nucleus. *Arrowheads* indicate condensate-like foci. Note the higher concentration of condensates in the nucleus than in the cytoplasm. The *inset* in the *upper right corner* shows a magnified detail from a single confocal plane. Scale bar: 10 μm.
Source data are available for this figure.

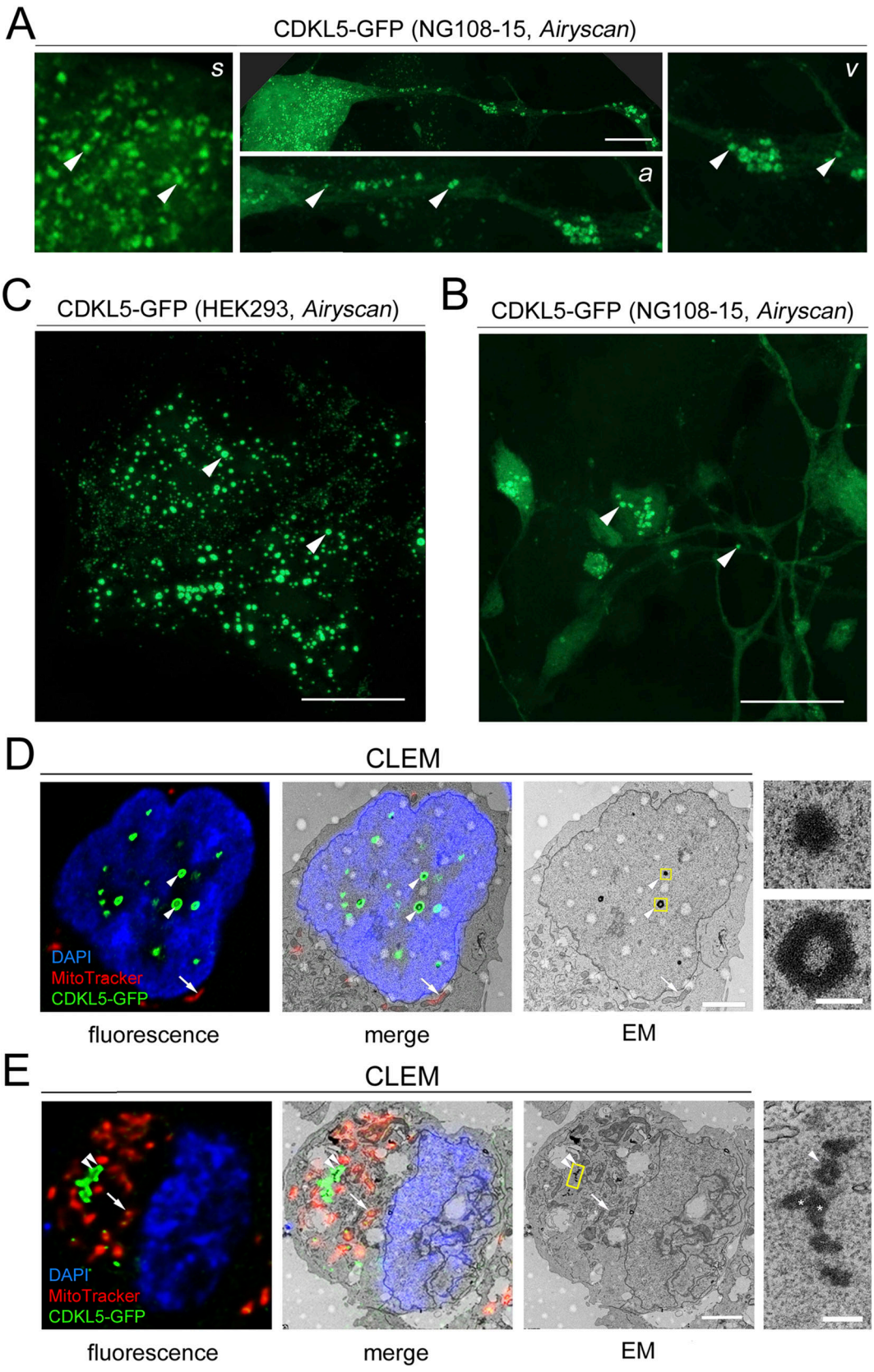

Figure 4. Exogenous CDKL5-GFP forms membraneless condensate-like foci in neuronal and nonneuronal cells.
(A) *Central upper panel.* Super-resolution (Airyscan, Zeiss) confocal fluorescence micrograph of a differentiated NG108-15 neuronal cell expressing CDKL5-GFP. The *left*, *lower middle*, and *right panels* show, respectively, magnified details of the somatic compartment (*s*), the axon (a), and a varicosity (*v*). Note the intra- and

undergo spontaneous condensation of GFP-tagged full-length (FL) CDKL5 (as a positive control), of its two major NTD and CTD fragments, and of GFP alone (as a negative control), in both neuronal and nonneuronal cells (Fig 6A and B).

When we compared the cell area occupied by condensates in transfected cells of the four experimental groups, we observed significant overall differences in a one-way ANOVA statistical analysis ($F_{(3,105)}$ = 19.61, P < 0.001; Fig 6C and D). Pairwise post hoc comparisons between the groups revealed that the CTD fragment displayed significant condensation compared with the GFP-negative control group (42.45% ± 4.86%, n = 31 microscopy fields, versus 5.80% ± 3.42%, n = 11, respectively; values normalized to the mean of the FL CDKL5-positive control group; P < 0.04, NK test), similar to what observed for the FL protein (100% ± 12.25%, n = 35; P < 0.001 versus the GFP group, NK test). Conversely, the NTD group, while displaying noticeable formation of large condensates in some cells, did not show a significant difference from the GFP group (relative condensate area in cells, 22.72% ± 6.15%, n = 32, values normalized to the FL group, P = 0.24, NK test). Both the CTD and the NTD displayed significantly lower condensation rates compared with the FL protein (P < 0.001 in both cases), based on the analysis of the cell area occupied by condensates. Although the individual condensates were on average larger for both the NTD and the CTD, in comparison with the FL group ($F_{(2,12541)}$ = 63.11, P < 0.001; FL 100% ± 1.43%, n = 9,709 condensates, versus NTD 146.5% ± 6.02%, n = 1,252, and versus CTD 127.49% ± 4.69%, n = 1,583, P < 0.001 in both instances, NK test; Fig 6D), they were also significantly fewer ($F_{(3,105)}$ = 30.63, P < 0.0001; FL: 100% ± 10.8%, n = 35 microscopy fields, versus NTD: 16.35% ± 5.23%, n = 32, and versus CTD: 32.11% ± 3.45%, n = 31 microscopy fields; P < 0.001 in both instances, NK test; Fig 6C). These quantitative parameters together indicate that LLPS nucleation efficiency is higher for the full-length protein, whose condensation occurs at numerous sites within cells, rather than for its fragments, especially the NTD, which condensate more sporadically, although their individual condensates may grow larger. The latter phenomenon may arise from the increased availability in the cellular environment of soluble NTD or CTD protomers that can be recruited within the few active condensation centers.

We also tested the relative ability of the NTD and the CTD fragments to undergo rapid, triggered LLPS using the optoDroplet system (Shin et al, 2017), an optogenetic tool allowing to photo-trigger the condensation of LLPS-prone proteins/peptides in a spatially and temporally controlled manner in the cellular environment (Fig 6E). In these experiments, either the NTD or the CTD was expressed in cells in fusion with the red fluorescent protein mCherry (mCh), for protein visualization, and an *A. thaliana* Cry2 fragment (mCh-Cry2) to confer photoactivability to the phase separation process (Shin et al, 2017; Fig 6F). mCh-Cry2 alone was expressed in control cultures (Fig 6F). In these experiments, we did not test the LLPS behavior of the full-length protein in fusion with mCh-Cry2 as its already massive spontaneous phase separation would occlude further increases in condensation upon photoactivation.

Cell cultures expressing NTD-mCh-Cry2, CTD-mCh-Cry2, or mCh-Cry2 were either photoactivated using 488-nm blue light for 2 min (Shin et al, 2017; see the Materials and Methods section) or left untreated as a control, and then fixed at 2 (to test for LLPS induction) or 30 (to test for rapid LLPS reversibility) min after the end of photoactivation. For each construct, we quantified the relative proportion (%) of mCh-positive cell area occupied by condensates in cultures that were either photoactivated ("+") or not ("−", *control*; Fig 6F and G). A two-way ANOVA revealed overall significant effects of the expressed protein ($F_{(2,414)}$ = 123.61, P < 0.001), photoactivation ($F_{(2,414)}$ = 90.81, P < 0.001), and their interaction ($F_{(4,414)}$ = 68.83, P < 0.001; n = 44–48 microscopy fields per group). Post hoc comparisons showed that the mCh-Cry2 control protein alone did not undergo significant condensation after photoactivation, as expected (P = 0.96, NK post hoc test). Conversely, the CTD-mCh-Cry2 fusion protein displayed, even under basal conditions, some degree of spontaneous condensation, which was strongly increased upon photoactivation (P < 0.001, NK post hoc test). NTD-mCh-Cry2 instead displayed only a minimal, nonsignificant increase in condensation upon photoactivation (P = 0.67, NK post hoc test). The phototriggered condensation of the CTD was rapidly reversible, as typical of LLPS-driven processes (Vaglietti et al, 2023). Indeed, the condensation state of the CTD-mCh-Cry2 fusion protein was not different from that of control cultures 30 min after photoactivation (P = 0.17, NK post hoc test).

Taken together, these analyses indicate that the physiological condensation pattern of the full-length protein depends on the presence of both the NTD and the CTD, and that the latter appears to be primarily responsible for driving CDKL5 LLPS.

A defined serine-rich CTD internal fragment (CTIF) plays a pivotal role in driving LLPS

The CTD constitutes about two thirds of the entire CDKL5 protein, for a total of 663 residues in the isoform most expressed in the brain, encompassing residues 298–960. The previous findings prompted us to test whether the entire CTD is necessary to mediate LLPS or a specific subregion of it may play a more prominent role in driving this process.

extranuclear condensate-like foci (*arrowheads*). Scale bar: 10 μm. The image upper corners have been filled in dark gray for graphical purposes. **(B)** Neuropil of intermeshed neurites, with varicosities, of NG108-15 cells expressing CDKL5-GFP. *Arrowheads* indicate condensate-like CDKL5 foci in a varicosity (*left*) and along a neurite (*right*). Scale bar: 10 μm. **(C)** Two HEK293 cells expressing CDKL5-GFP. *Arrowheads* indicate condensates. Scale bar: 10 μm. **(D)** Correlative light and electron microscopy (CLEM) images of a HEK293 cell expressing CDKL5-GFP. The *first panel from the left* shows a confocal fluorescence image with intranuclear CDKL5-GFP condensates (*green*). The nucleus is stained with DAPI (*blue*), and mitochondria (*white arrow*) are marked by the MitoTracker dye (*red*). The *third panel* shows an EM image of a cell section at the same level of the confocal fluorescence image. The *second panel* is an overlay of the fluorescence and EM images. The two fluorescent condensate-like foci are highlighted by *arrowheads* and correspond to denser areas (boxed in *yellow* in the EM image) within the nuclear compartment, which are magnified in the two *right panels*. The MitoTracker signal overlaps with mitochondria, as expected. The two condensates are membraneless, and the larger one has an internal cavity also visible in the fluorescence image (see the Results section). Scale bars: 2.5 μm (larger images), 250 nm (smaller panels). **(E)** As in panel (D), for cytoplasmic condensate-like foci. The *fourth image on the right* illustrates a cluster of them (see *yellow box* in the EM image), two of which (*asterisks*) appear to be coalescing with each other. **(D)** Scale bars as in panel (D).

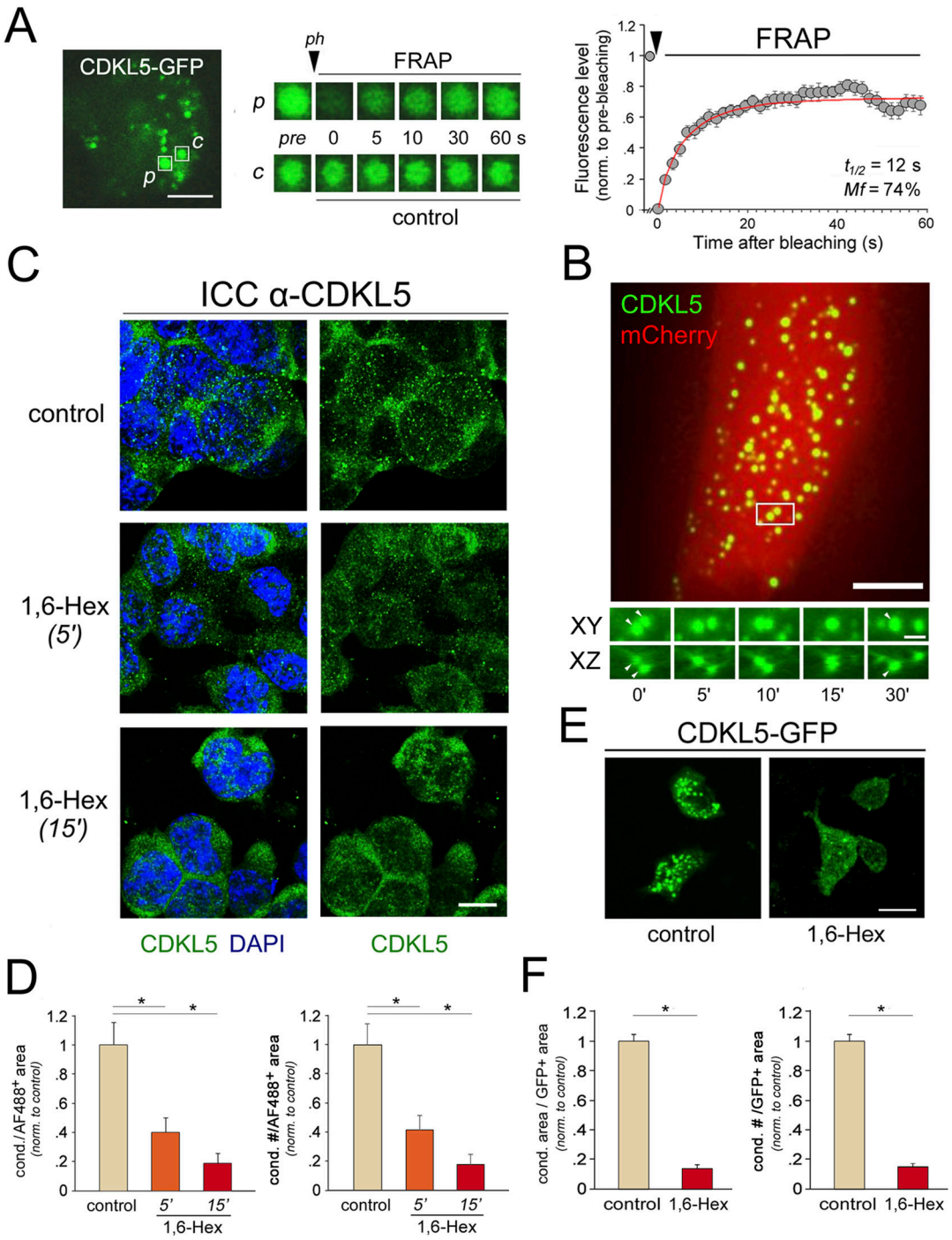

Figure 5. CDKL5 foci display hallmark features of LLPS-driven condensates.
(A) FRAP experiments on CDKL5 foci. The *left panel* shows a confocal image of a HEK293 cell expressing CDKL5-GFP. Scale bar: 5 μm. Two condensates are highlighted within *white squares*. One of them was photobleached (*p*), and the other one was used as a control (*c*). In the *middle section*, the *upper series* of time-lapse images displays the condensate *p* before (*pre*) and at the indicated times after photobleaching. Condensate *p* showed substantial fluorescence recovery within about a minute after photobleaching. For condensate *c* (*lower series*), which was not actively photobleached, only modest fluorescence bleaching was observed owing to repeated imaging. The *right graph* displays the mean FRAP time course for photobleached CDKL5-GFP foci (n = 11; half-time ($t_{1/2}$) = 12 s; mobile fraction (*Mf*) = 74%). **(B)** The *upper panel* displays a confocal image of a HEK293 cell cotransfected with two plasmids for the expression of CDKL5-GFP and mCherry (as a whole-cell marker). The image is part of a time-lapse series of images, as shown in Video 1, which were acquired to study the coalescence of CDKL5-GFP foci (scale bar: 5 μm). Note the presence of numerous rounded CDKL5-GFP foci of variable size. Two neighboring foci, highlighted within the *white box*, fuse during the time-lapse experiment. The two lower rows of magnified images (scale bar: 1 μm) display the coalescence of these two condensates into a larger one, with images taken at the indicated time intervals. The *upper row* shows the two foci on the XY plane. The *lower row* shows the same two foci in an orthogonal view (XZ plane) generated using the ImageJ "orthogonal views" function. **(C)** Confocal fluorescence images of NG108-15 cells immunostained to detect the distribution of endogenous CDKL5 (*green*). The DAPI *blue* signal in the *left column* of images marks cell nuclei. The cells were fixed after 5 or 15 min of 1,6-hexanediol (*1,6-Hex*) treatment. Mock-treated cells were used as the *control* group. Note how 1,6-Hex

In search of candidate LLPS-mediating CTD subregions, we considered that previous reports based on CDKL5 deletions indicated that residues between 525 and 781 have an important role in regulating the subcellular distribution of the protein (Ricciardi et al, 2009), which, from the perspective of our analysis, may also have to do with LLPS. Remarkably, we found that this region of the protein has substantial overlap with the longest uninterrupted stretch of residues, between 657 and 840, with very high LLPS propensity in the FuzDrop prediction diagram (P_{DP} score > 0.8; peak *3* in Fig 7A). Indeed, the average per-residue P_{DP} score in this region (0.93 ± 0.01, n = 184 residues) was significantly higher than the average score across residues of the upstream (CTDu; a.a. 298–656; 0.83 ± 0.01, n = 395 residues) and downstream (CTDd; a.a. 841–960; 0.86 ± 0.01, n = 120 residues) parts of the CTD, and of the NTD (0.33 ± 0.01, n = 297). A one-way ANOVA revealed a significant overall difference among the four protein segments ($F_{(3,956)}$ = 1,162.4, P < 0.001). Furthermore, pairwise post hoc tests highlighted significant differences between the 657–840 fragment and each one of the three other fragments, that is, CTDu, CTDd, and NTD (P < 0.001, NK test, in all instances; Fig 7B).

Thus, we hypothesized that this CTD internal fragment (CTIF) may play a pivotal role in driving LLPS. To test this hypothesis, we expressed, in both neuronal and nonneuronal cells, a GFP-tagged form of CDKL5 devoid of the CTIF (CDKL5-ΔCTIF; Fig 7C) and assessed whether such an internal deletion may impact the ability of the protein to form intracellular condensates. We found that CDKL5-ΔCTIF was still able to form condensates, but to a significantly lower extent than wild-type (WT) CDKL5 in both neuronal and nonneuronal cells (Fig 7D). In both cell types, the protein appeared to condensate more frequently in the nuclear compartment. A one-way ANOVA indicated overall significant differences between the experimental groups in HEK293 cells for both condensate area ($F_{(2,114)}$ = 80.21, P < 0.0001; Fig 7E) and condensate number ($F_{(2,114)}$ = 51.90, P < 0.0001). Indeed, the CDKL5-ΔCTIF condensates occupied a significantly lower proportion of the cellular area than the condensates formed by WT CDKL5 (29.6% ± 3.88%, n = 48 microscopy fields, versus 100% ± 7.17%, n = 44; P < 0.01, NK post hoc test; values normalized to the WT CDKL5 group). This decrease in total condensate area displayed by CDKL5-ΔCTIF was paralleled by a decrease in the number of condensates formed by this mutant (34.63% ± 7.05%, n = 48 microscopy fields, versus 100% ± 6.37%, n = 44; P < 0.001, NK post hoc test; values normalized to the WT CDKL5 group), and was accompanied by a moderate increase in the mean size of individual condensates (110.99% ± 2.84%, n = 1,179 condensates, versus 100% ± 1.47%, n = 3,894, P < 0.001, *t* test; values normalized to the WT CDKL5 group).

To further confirm the LLPS propensity of the CTIF alone, we studied its ability to undergo rapid phototriggered phase separation when expressed in HEK293 cells as a CTIF-mCh-Cry2 fusion protein (Fig 7F). In live-cell experiments, we found that the CTIF-mCh-Cry2 fusion was able to undergo robust LLPS upon photoactivation, which was not observed under the same conditions in control cells expressing mCh-Cry2 alone (Fig 7G). A one-way ANOVA for repeated measures indicated significant overall differences between the two experimental groups in terms of expressed construct, time, and their interaction ($F_{(20,1020)}$ = 69.38, P < 0.0001). Post hoc tests indicated that photoactivation induced significant condensation of mCh-Cry2–tagged CTIF in comparison with basal conditions (peaking at 2 min after photoactivation; P < 0.001, NK test) but not of mCh-Cry2 alone (P = 0.81). Remarkably, the CTIF-mCh-Cry2 condensation was reversible, as typical of LLPS-driven processes (e.g., Vaglietti et al, 2023), rapidly decreasing toward baseline levels within 10–15 min.

Taken together, these findings indicate that the serine-rich CTIF represents a key player in the phase transitions of CDKL5. As the CDKL5-ΔCTIF was still able to condensate to a limited extent, the other parts of the CTD and/or the NTD must also play a role in CDKL5 LLPS.

The CTD is mostly affected by nonsense and frameshift pathogenic mutations which may lead to the production of C-terminally truncated CDKL5 forms with variable loss of LLPS-prone regions

Based on the previous findings, we sought to analyze the distribution of known disease-related mutations of the *CDKL5* gene to identify those that may target the CTD, and in particular the CTIF, which could potentially interfere with the LLPS behavior of the protein.

The NTD and CTD of CDKL5 are differentially targeted by distinct types of pathogenic mutations, as previously observed (Hector et al, 2017). Indeed, while the NTD is affected by missense, nonsense, and frameshift mutations, the CTD is almost exclusively targeted by the latter two types of mutations. We analyzed quantitatively how the type and frequency of disease-related coding mutations affecting these different portions of the CDKL5 protein vary. Toward this aim, we first derived a list of coding mutations, categorized as pathogenic, from the *ClinVar* database that either introduce premature termination codons (PTCs) potentially leading to the production of truncated forms of CDKL5 (i.e., nonsense and frameshift truncating mutations, TMs), or instead cause single amino acid substitutions (missense) or in-frame insertion/deletions (i.e., nontruncating mutations, NTMs; Table S2; Fig 8A). Then, we calculated the relative proportion of TMs and NTMs that affect the two main CDKL5 domains (Fig S5A). These

rapidly promotes the dissolution of CDKL5 foci. Scale bar: 10 μm. **(C, D)** Quantification of the effect of 1,6-Hex on endogenous CDKL5 condensate-like foci, as shown in panel (C). The mean CDKL5-positive (as stained using Alexa Fluor 488 (AF488)–conjugated secondary antibodies) area occupied by these structures (*left graph*), and their average number per AF-488-positive cell area (*right graph*) is significantly reduced by 1,6-Hex. In both graphs, values are normalized to the mean values of the respective control groups. *Asterisks* indicate statistically significant differences. **(E)** Confocal fluorescence images of HEK293 expressing CDKL5-GFP (*green*). The image *on the right* shows cells fixed after 15 min of 1,6-Hex treatment. Untreated *control* cells are shown *on the left*. Note how 1,6-Hex rapidly promotes the dissolution of condensate-like CDKL5-GFP foci. Scale bar: 10 μm. **(E, F)** Quantification of the effect of 1,6-Hex, as shown in panel (E). The mean proportion of the CDKL5-positive area occupied by condensate-like foci (*left graph*) and their average number per GFP-positive cell area (*right graph*) are significantly reduced by 1,6-HEX. In both graphs, values are normalized to the mean values of the respective control groups. *Asterisks* indicate statistically significant differences.
Source data are available for this figure.

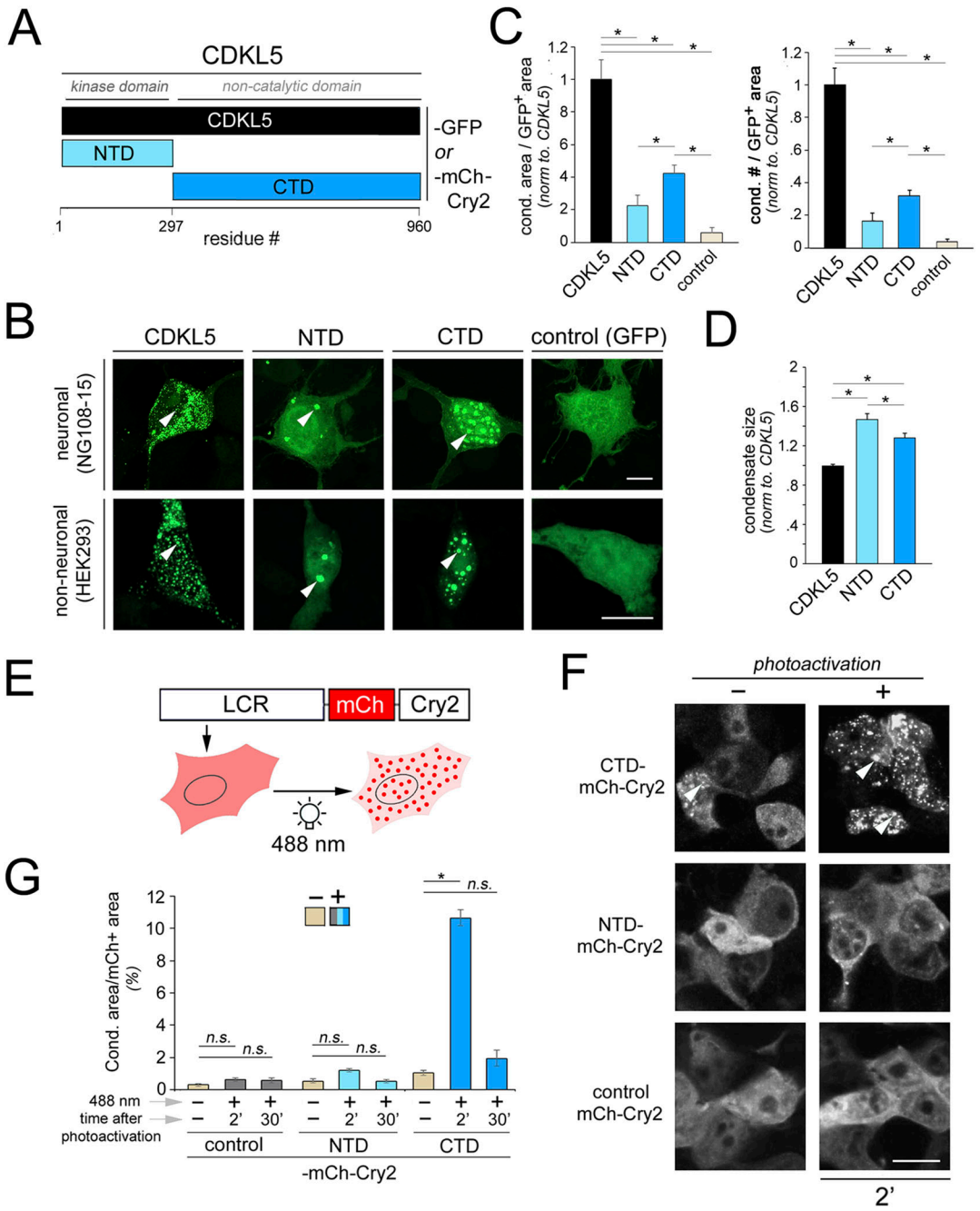

Figure 6. CDKL5 condensation is primarily driven by its C-terminal domain (CTD).
(A) Schematic representation of constructs for the cellular expression of full-length CDKL5 (*black*), and of its N-terminal domain (NTD) (*cyan*), or CTD (*turquoise*), as fusion proteins with either GFP or mCh-Cry2 for the study of spontaneous and triggered LLPS, respectively. **(B)** GFP-tagged CDKL5, its NTD or CTD fragments, or GFP alone was expressed in neuronal (differentiated NG108-15, *upper row*) and nonneuronal (HEK293, *lower row*) cells to study their spontaneous condensation (*arrowheads* indicate condensates). Although CDKL5-GFP forms a myriad of small condensates, the NTD displays only a few larger ones, whereas the CTD forms numerous condensates of intermediate size that are often concentrated in the nucleus, especially in NG108-15 cells. Scale bars: 10 μm. **(B, C)** Quantification of the spontaneous condensation (total condensate area per GFP-positive cell unit area (*left graph*) and condensate number per GFP-positive cell area (*right graph*) of the different constructs expressed in HEK293 cells as shown in panel (B). Values are normalized to the mean of the CDKL5-GFP group in both graphs. *Asterisks* indicate statistically significant differences. **(D)** As in (C), for the average size of individual condensates. **(E)** Schematic representation of the optoDroplet system for studying rapidly triggered LLPS (Shin et al, 2017). Cell cultures expressing an LLPS-prone peptide of interest, such as an LCR, in fusion with mCh-Cry2, and control cultures expressing mCh-Cry2 alone are illuminated with blue light (488 nm) to optically trigger the rapid formation of condensates ("optoDroplets," i.e., the *red dots* in the right cell). Control cultures expressing mCh-Cry2 display negligible condensation upon photoactivation. mCh fluorescence is used to monitor the fusion protein localization. **(F)** Confocal fluorescence images of cell cultures expressing CDKL5 NTD or CTD fused to mCh-Cry2, or mCh-Cry2 alone (*control*). For each expressed construct, some cultures were photoactivated by a 2-min pulse of 488-nm blue light (*right column*, "+") and fixed 2 min after, whereas other control cultures were not photoactivated (*left column*, "–") and fixed at the same time of the photoactivated cultures. Other cultures were fixed at 30 min after the photoactivating pulse to check for condensation reversibility. *Arrowheads* indicate condensates. Scale bar: 10 μm. **(F, G)** Bar graph showing the proportion (%) of the mCh-positive cell area occupied by condensates in cell cultures treated as shown in panel (F). For each indicated construct, condensation was quantified in control, nonphotoactivated cultures (basal spontaneous condensation), and

findings confirmed previous observations that the CTD is essentially affected almost entirely by TMs, whereas the NTD is targeted by both types of mutations (Fig 8A). The differential distribution of TMs and NTMs across the NTD and the CTD is statistically significant ($P < 0.01$, Fisher's exact test; Fig S5A). Interestingly, 29.7% (75/252) of TMs affect the most LLPS-prone regions of the CTD, that is, the CTIF (a.a. 657–840) and the downstream tail of the protein (a.a. 841–960). Interestingly, the only pathogenic NTM in the CTD (c.2152G>A) targets the CTIF-coding region (Fig 8A). In principle, this may appear as a missense mutation, causing a single amino acid substitution (V718M). However, Hector et al (2017) observed that the mutation leads to a splicing defect, with skipping of exon 14 (r.2047_2152del), and the appearance of a downstream PTC in exon 14, which encodes a portion of the LLPS-driving region of the CTD.

Premature termination codons (PTCs), such as those produced by nonsense and frameshift mutations in CDKL5 transcripts, can trigger NMD (Torene et al, 2024), which prevents the production of C-terminally truncated mutant CDKL5 proteins. However, transcripts with PTCs in the distal portion of their open reading frame (ORF) may escape NMD and be translated into truncated proteins (Torene et al, 2024). Similarly, transcripts bearing PTCs near the initial part of the ORF can also escape NMD with downstream translation reinitiation producing N-terminally truncated proteins (e.g., Paulsen et al, 2006). Moreover, even a significant portion (~30%) of mutations predicted to trigger NMD can escape it (Torene et al, 2024), also based on local RNA sequence context (Embree et al, 2022) and cell type–specific mechanisms. Indeed, NMD efficiency is relatively low in postmitotic cells, such as neurons (Palou-Márquez & Supek, 2025).

No systematic analysis exists of NMD efficiency for PTCs positioned along the entire length of the CDKL5 ORF, and the expression level of transcripts bearing nonsense/frameshift CDKL5 mutations is largely unknown (Hector et al, 2017). However, Bahi-Buisson et al (2008) found that transcripts bearing distal PTCs encoding truncations at residues 693 and 799 of the protein escape NMD in patient-derived cells. Moreover, Feng et al (2025), in gene-edited mouse cell lines, recently reported the expression of CDKL5 protein truncated at residues 862 and 866. These findings indicate that distal PTCs in CDKL5 transcripts, at least downstream of codon 692, may escape NMD (Fig 8A, highlighted in *red*), consistent with what is generally observed in other genes in recent systematic screenings (Torene et al, 2024).

Remarkably, the C-terminally truncated proteins produced from the translation of NMD-escaping transcripts would lack variable portions of the LLPS-driving region of the CTD. This indicates that even the most distal portions of this domain are important for CDKL5 function, and that their loss can be pathogenic despite the presence of an intact catalytic NTD. These findings strongly suggest that distally truncated forms of the CDKL5 protein may exhibit an altered LLPS behavior.

The possible functional relevance of the most C-terminal portion of the CTD is also suggested by analyses of the predicted impact of pathogenic missense mutations performed using AlphaMissense ("αM" in Fig 8B; Cheng et al, 2023) and evolutionary analyses. Indeed, αM identifies multiple regions in the CTIF and flanking regions of the CTD in which amino acid substitutions are predicted to be deleterious and potentially pathogenic, just like those falling within the kinase domain. Remarkably, these sequences correspond to the regions with very low per-site evolutionary entropy within the CTD in an alignment of the primary sequences of CDKL5 orthologs of six gnathostome vertebrate species ranging from *Danio rerio* (Actinopterygii) to *Homo sapiens* (Euarchontoglires; Fig 8B, entropy [*Ent*] graph, *arrowheads*).

Disease-related distal truncations deleting the CTIF and the downstream portion of the CTD tail reduce LLPS and catalytic activity of CDKL5

To test the possible biological effects of distal CTD truncations on CDKL5 LLPS, we studied two CTIF-targeting pathogenic mutations, that is, S726X and R781X (Bertani et al, 2006; Rusconi et al, 2008; Trump et al, 2016). Although their expression levels have not been directly measured in previous reports (Bertani et al, 2006; Rusconi et al, 2008; Trump et al, 2016), the CDKL5 transcripts bearing these mutations may escape NMD, leading to the production of CDKL5-S726X and CDKL5-R781X truncated proteins, based on the previous analyses of NMD escape in *CDKL5* and other genes (Bahi-Buisson et al, 2008; Torene et al, 2024; Feng et al, 2025). We used these two mutant proteins as representative cases for a class of disease-related CDKL5 distal truncations deleting variable portions of the LLPS-driving region of the CTD (Fig 9A). CDKL5-S726X and CDKL5-R781X lack, respectively, ~2/3 and ~1/3 of the CTIF together with the more distal tail of the CTD (a.a. 726–960 and 781–960, respectively).

To test the possible impact of the two mutations on CDKL5 LLPS behavior, we compared the relative ability to undergo LLPS of GFP-tagged WT CDKL5, its two truncated mutants CDKL5-S726X and CDKL5-R781X, and GFP alone as a negative control (Fig 9B). The WT and mutant proteins were expressed in cells after transfection with equimolar amounts of the plasmids encoding them. Under these conditions, the CMV promoter-driven vector that we used led to a 12-fold increase in the expression level of the CDKL5 protein as compared to its endogenous levels (12.04 ± 2.47 versus 1 ± 0.35, n = 3 per group, $P < 0.02$, *t* test; Fig S5B), in the range of what was previously found using similar vectors (e.g., Burstein et al, 2018). The expression levels were not different between WT and mutant forms of the protein (Fig S5C; $F_{(2,9)} = 0.35$, $P = 0.70$, one-way ANOVA). We found that both deletion mutants displayed a significant reduction in spontaneous condensation in comparison with full-length WT CDKL5 (Fig 9C). Indeed, a one-way ANOVA showed an overall significant difference between the experimental groups in both total condensate area ($F_{(3,225)} = 30.64$, $P < 0.001$) and number

in cultures that were photoactivated (triggered condensation) and fixed at either 2 or 30 min after photoactivation. *Asterisks and "n.s."* indicate statistically significant and nonsignificant differences, respectively, between experimental groups of interest. Note that only the CTD construct undergoes a significant induction of condensation at 2 min after photoactivation. Such condensation is reversible and essentially disappears within 30 min. Scale bar: 5 μm.
Source data are available for this figure.

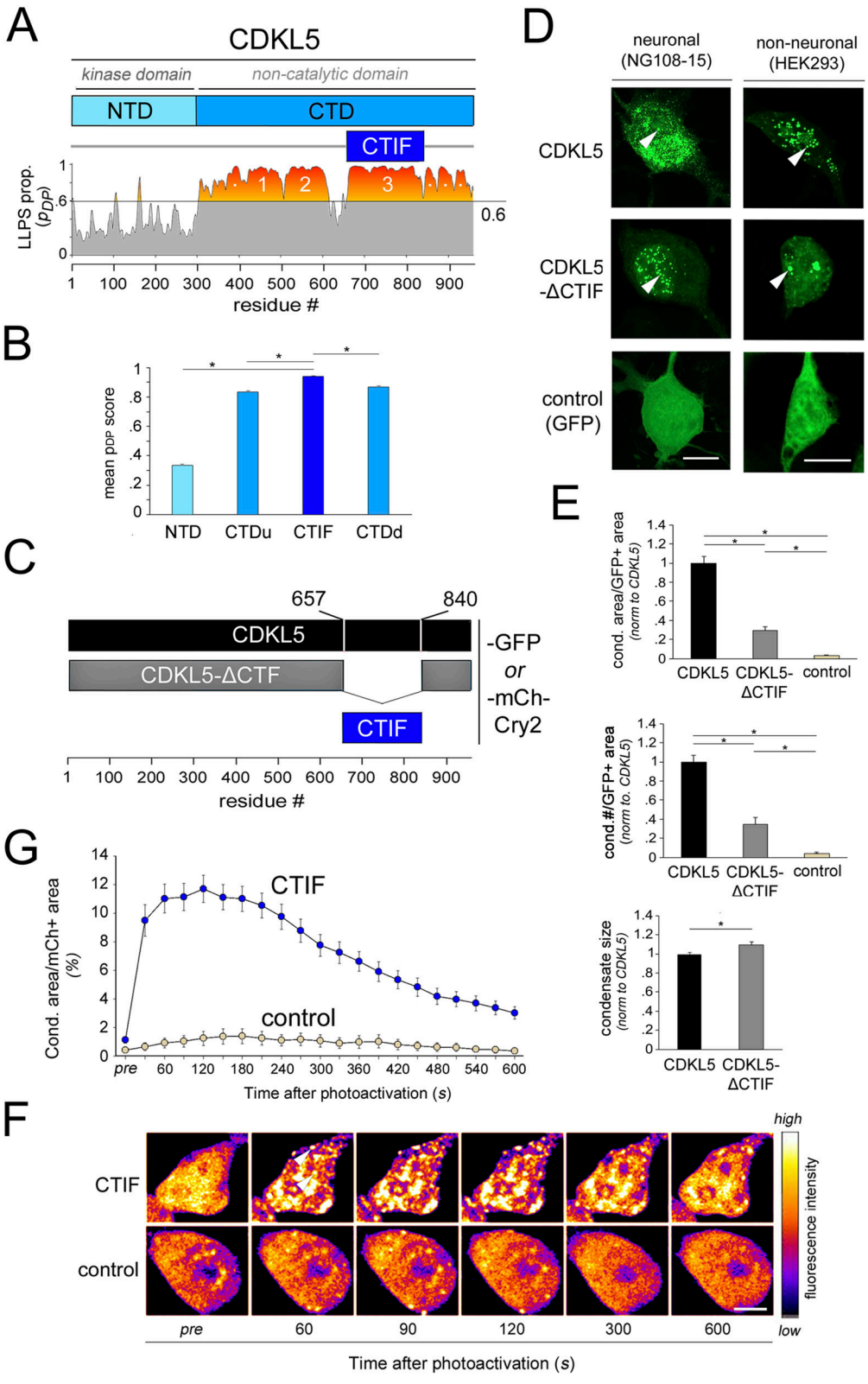

Figure 7. A C-terminal internal fragment (CTIF) of the CTD has a key role in driving CDKL5 LLPS.
(A) The *upper bar* displays a schematic representation of the CDKL5 primary sequence. The N-terminal domain is highlighted in *cyan* and the CTD in *turquoise*. The *lower graph* plots the FuzDrop per-residue LLPS propensity score (P_{DP} score) along the primary sequence of human CDKL5. The area under the curve with the above-threshold LLPS propensity (P_{DP} score > 0.6) is highlighted in *orange/red*. The *blue bar* tract identifies a C-terminal internal fragment (CTIF; a.a. 657–840) of CDKL5 corresponding to the longest uninterrupted region of the CTD with very high (>0.8) P_{DP} score (i.e., peak 3; see Fig 3A). **(B)** Bar graph plotting the mean P_{DP} score across residues of the N-terminal domain (a.a. 1–297), the CTIF (a.a. 657–840), and the two upstream (*u*) and downstream (*d*) CTD portions, that is, CTDu (a.a. 298–656) and CTDd (a.a. 841–960), respectively. Note how the CTIF has the highest mean LLPS propensity score. **(C)** Schematic representation of the constructs that were generated for the cellular expression of full-length CDKL5 (*black*), or a CTIF deletion mutant (CDKL5-ΔCTIF, *gray*), or the CTIF alone (*blue*), as fusion proteins with either GFP or mCh-Cry2 for the study of spontaneous and triggered LLPS, respectively. **(D)** GFP-tagged CDKL5, its CDKL5-ΔCTIF deletion mutant, or GFP alone as a control were expressed in neuronal (differentiated NG108-15, *left column*) and nonneuronal (HEK293, *right column*) cells to study their spontaneous tendency to form condensates (*arrowheads*). CDKL5-ΔCTIF can still form condensates in both cell types, although at a significantly lower level than the full-length CDKL5 protein. Scale bars: 10 μm. **(E)** Quantification of the spontaneous condensation of the different constructs expressed in HEK293 cells, as shown in panel (D), as the mean proportion of the GFP-positive cell area occupied by condensates (*upper graph*), the mean number of condensates per GFP-positive cell area (*middle graph*), and the mean size of individual condensates (*lower graph*). Values are normalized to the mean of the CDKL5-GFP group in each graph. *Asterisks* indicate significant differences. CTIF deletion significantly reduces condensation overall. **(F)** Confocal fluorescence images of cell cultures expressing either CTIF-mCh-Cry2 or mCh-Cry2 alone (*control*) at the indicated time points before (*pre*) and after photoactivation in live-cell imaging experiments. Photoactivation induces massive condensation of CTIF-mCh-Cry2 (but not of mCh-Cry2 alone), which peaks at 2 min after the end of the 488-nm light pulse and starts declining at later time points. *Arrowheads* indicate condensates. Fluorescence intensity is represented using the pseudocolor scale shown *on the right*. **(G)** Graph plotting the mean proportion of mCh-positive cell area occupied by condensates in cells expressing CTIF-mCh-Cry2 or mCh-Cry2 at the indicated time points during live-cell optoDroplet induction experiments, as shown in panel (F). Source data are available for this figure.

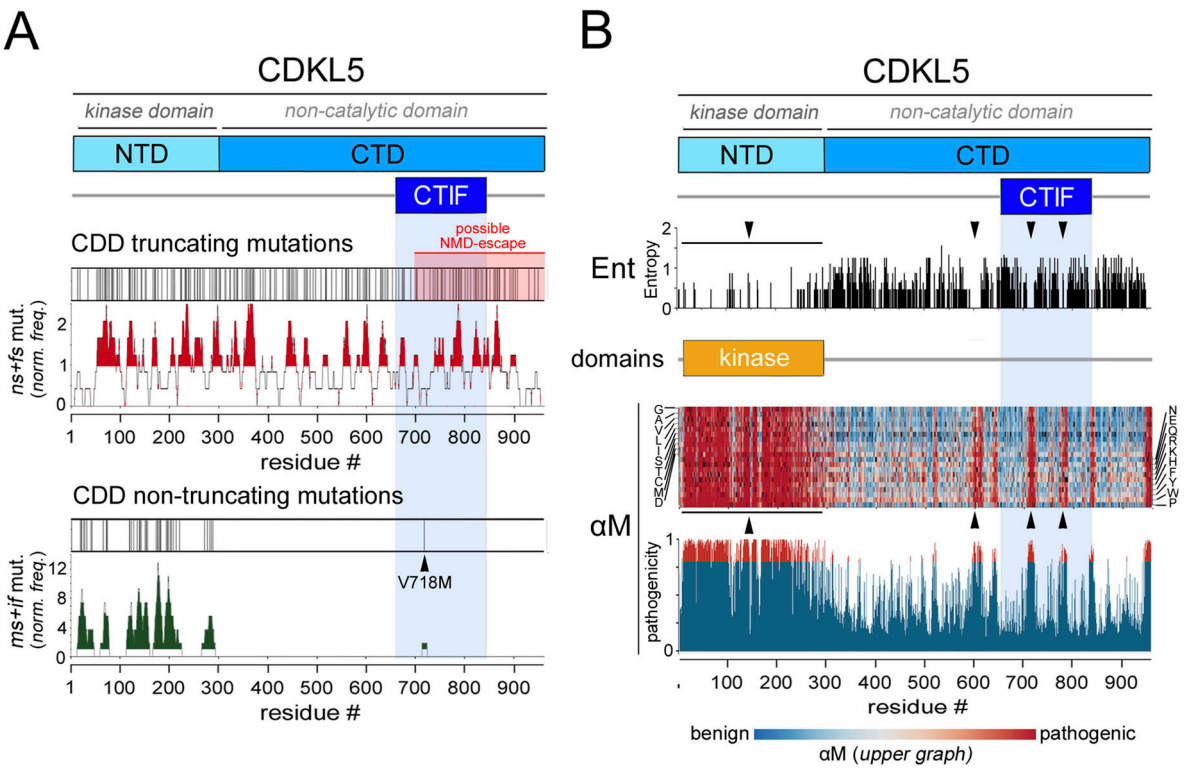

Figure 8. Analysis of the distribution and predicted pathogenic impact of truncating and nontruncating mutations of CDKL5.
(A) *Upper two bars*. Schematic representation of the CDKL5 protein with the N-terminal domain (NTD; *cyan*), the C-terminal domain (CTD; *turquoise*), and the CTIF (*blue*). Below, the *thin vertical lines* on the two white bars represent, as indicated, the positions of truncating (nonsense (*ns*) and frameshift (*fs*)) or nontruncating (missense (*ms*) and in-frame indel (*if*)) disease-related coding mutations along the CDKL5 open reading frame (ORF) as reported in *ClinVar*. The *graphs below* the white bars plot the local frequency of truncating and nontruncating disease-related mutations, as calculated in a sliding window of 21 triplets centered around each codon of the CDKL5 ORF. Values are normalized to the mean occurrence of the two types of mutations along the entire ORF. Above-average (>1) frequency peaks are highlighted in *red* and *dark green*, respectively, for truncating and nontruncating mutations. Note how, although disease-related truncating mutations can affect the protein along its entire length, missense mutations target essentially the NTD, as also observed previously (Hector et al, 2017). The truncating mutations targeting the distal portion of the CTD (highlighted in *red*) may lead to the production of truncated proteins as the mutant transcripts can escape nonsense-mediated decay (see the *Results* and *Discussion* sections). Remarkably, the only disease-related missense mutation targeting the CTD (V718M) affects the CTIF. This mutation may cause splicing defects (Hector et al, 2017). **(B)** *Upper two bars*. Schematic representation of the CDKL5 protein with the NTD (*cyan*), the CTD (*turquoise*), and the CTIF (*blue*). The entropy (Ent) calculated for each residue in an alignment of six vertebrate orthologs of CDKL5 (see the *Materials and Methods* section), and the position of the kinase domain ("domains") are reported below. The two bottom panels represent AlphaMissense (*α*M) predictions of the potential pathogenicity of the indicated amino acid substitutions at each position of the CDKL5 primary sequence (*upper panel*) and the overall per-residue pathogenicity score calculated by the algorithm (*lower panel*). Note how many LLPS-prone regions within the CTIF and flanking parts of the CTD are characterized by high pathogenicity scores and low entropy (i.e., a high degree of evolutionary conservation), similar to what found for most of the kinase domain, suggesting functional relevance.
Source data are available for this figure.

($F_{(3,225)}$ = 28.16, P < 0.0001). Post hoc tests indicated that the cell area occupied by condensates was significantly lower for both CDKL5-S726X (54.89% ± 4.34%, n = 92 microscopy fields; P < 0.001, NK test) and CDKL5-R781X (69.11% ± 6.19%, n = 34; P < 0.01, NK test) in comparison with full-length WT CDKL5 (100% ± 5.39%, n = 87, values normalized to the mean of the *wt* CDKL5 group). Both mutants still displayed significant condensation in comparison with the negative control group (GFP; P < 0.001, NK test, in both instances). The CDKL5-S726X mutant underwent a ~14% greater reduction in condensation in comparison with the other mutant CDKL5-R781X. Although this difference is not significant (P = 0.16, NK test), it suggests that a larger CTD deletion may cause a more pronounced LLPS impairment. The overall reduction in the total area occupied by condensates in cells expressing the two CDKL5 mutants was essentially related to a reduction in their number, without significant changes in their mean individual size (Fig 9C). Indeed, post hoc tests indicated that the number of condensates per GFP-positive unit area was significantly lower for both CDKL5-S726X (60.45% ± 4.78%, n = 92 microscopy fields; P < 0.001, NK test) and CDKL5-R781X (59.60% ± 5.05%, n = 34; P < 0.001, NK test) in comparison with full-length WT CDKL5 (100% ± 5.40%, n = 87, P < 0.001, NK test, values normalized to the mean of the *wt* CDKL5 group). In contrast, no significant difference was observed when comparing the average size of the condensates formed by CDKL5-S726X and CDKL5-R781X with that of WT CDKL5 condensates ($F_{(2,34546)}$ = 0.75, P = 0.47, one-way ANOVA). These observations indicate that the more or less complete loss of the CTIF (a.a. 657–840), together with the distal C-terminal portion of the CTD (a.a. 841–960), significantly impairs CDKL5 LLPS.

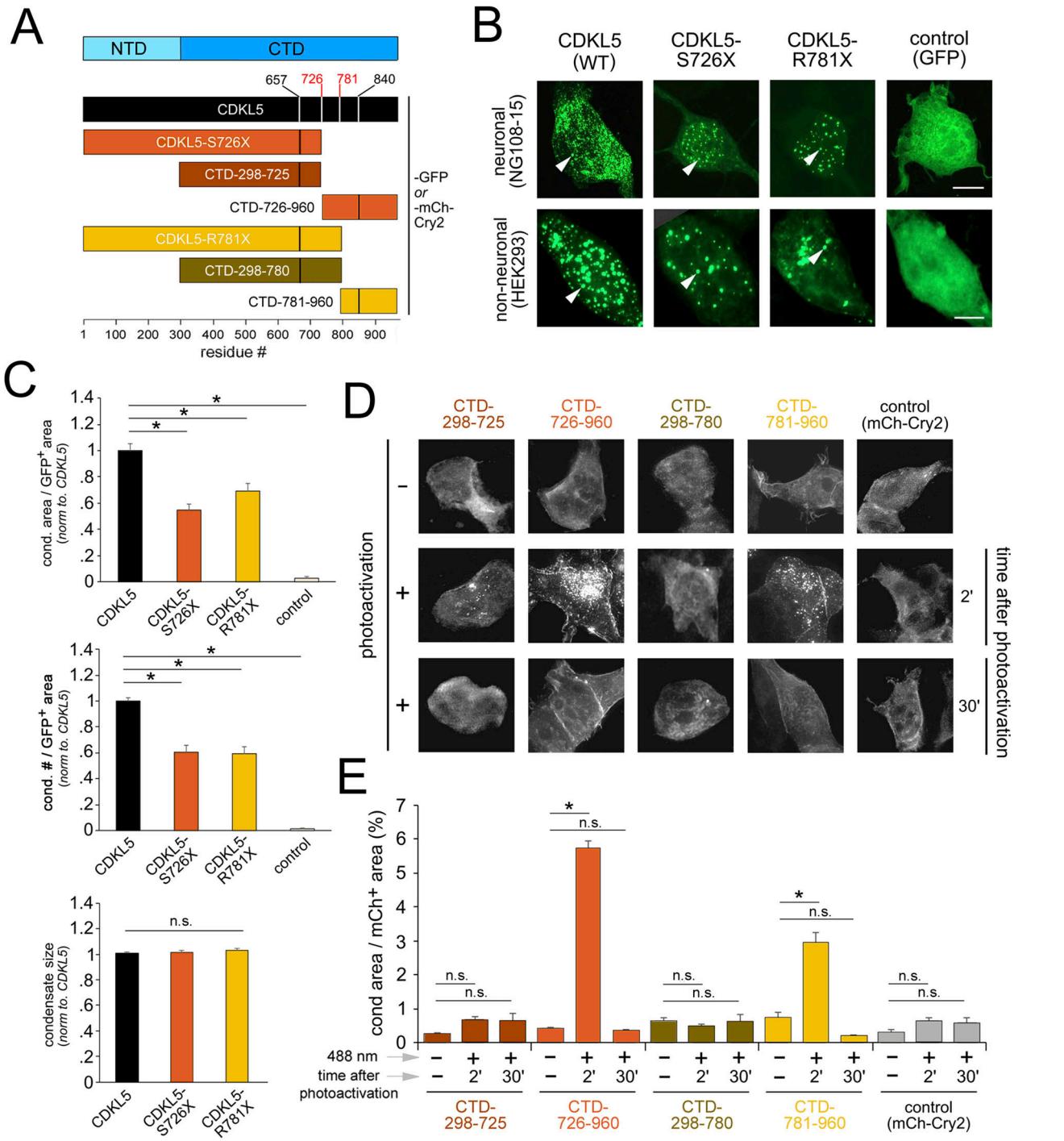

Figure 9. Mutations truncating the CDKL5 protein within the CTIF impair its LLPS.
(A) Schematic representation of the constructs that were generated for the cellular expression, as fusion proteins with either GFP or mCh-Cry2, of WT CDKL5 (*black*), two of its disease-related mutants (CDKL5-S726X and CDKL5-R781X), the two C-terminal tails of the C-terminal domain (CTD) (i.e., $CTD_{726–960}$ or $CTD_{781–960}$) deleted by the two mutations, or the corresponding upstream fragments of the CTD (i.e., $CTD_{298–725}$ or $CTD_{298–780}$). **(B)** GFP-tagged CDKL5, its two disease-related mutants, or GFP alone were expressed in neuronal (NG108-15, *upper row*) and nonneuronal (HEK293, *lower row*) cells to study their spontaneous tendency to condensate (*arrowheads*). Scale bars: NG108-15: 10 μm; HEK293: 5 μm. **(C)** Quantification of the spontaneous condensation of the indicated constructs in HEK293 cells, as shown in panel (B), expressed as the mean proportion of the GFP-positive cell area occupied by condensates (*upper graph*), the mean number of condensates per GFP-positive cell area (*middle graph*), and the mean size of individual condensates (*lower graph*). Values are normalized to the respective mean values in the CDKL5-GFP group. *Asterisks* indicate statistically significant differences. **(D)** Confocal fluorescence images of cell cultures expressing the indicated mCh-Cry fusion proteins or mCh-Cry2 alone (*control*). For each expressed construct, some cultures were photoactivated with 488-nm blue light (*middle and lower rows*, "+"), whereas control cultures were not photoactivated (*upper row*, "–"). Photoactivated cultures (+) were fixed at either 2 or 30 min after photoactivation to assess, respectively, LLPS induction and reversibility. *Arrowheads* indicate condensates. Scale bar: 5 μm. **(E)** Bar graph showing the proportion of the mCh-positive cell area occupied by condensates in cultures treated as shown in panel (D). For each indicated construct, condensation was quantified in control, nonphotoactivated cultures (basal spontaneous condensation), and in cultures that were

Consistent with this view, we found that the C-terminal fragments, that is, $CTD_{726–960}$ and $CTD_{781–960}$ (Fig 9A), which are deleted in the two S726X and R781X truncated mutants, were both able to undergo condensation in the optoDroplet assay, unlike the corresponding upstream fragments of the CTD (i.e., $CTD_{298–725}$ and $CTD_{298–780}$, respectively; Fig 9D). A two-way ANOVA (Fig 9E) indicated overall significant differences between the experimental groups in terms of expressed protein ($F_{(4,657)}$ = 61.85, P < 0.0001), treatment (photoactivation; $F_{(2,657)}$ = 167.38, P < 0.0001), and their interaction ($F_{(8,657)}$ = 75.63, P < 0.0001). Post hoc tests indicated that photoactivation was able to induce significant condensation of both the mCh-Cry2–tagged $CTD_{726–960}$ and the $CTD_{781–960}$ fragments (P < 0.0001 in both instances versus the respective nonphotoactivated control groups, NK test) but not of mCh-Cry2 alone (control group, P = 0.73), nor of the two upstream CTD fragments ($CTD_{298–725}$, P = 0.63 and $CTD_{298–780}$, P = 0.92 versus the respective nonphotoactivated control groups, NK test) at 2 min after photoactivation. Notably, the degree of condensation induced by photoactivation was significantly higher for the longer CTD terminal fragment ($CTD_{726–960}$) than for the shorter one ($CTD_{781–960}$; P < 0.0001, NK test). As expected, the condensation of both protein fragments was rapidly reversible and reached baseline values within 30 min after photoactivation. Indeed, the condensation level at 30 min was not significantly different than in nonphotoactivated control cultures for both fragments (P = 0.72 and P = 0.39, respectively, NK test).

These findings indicate that disease-related CTD truncations, by deleting the CTIF and the most distal portion of the protein (a.a. 841–960), can substantially alter the LLPS behavior of CDKL5 and therefore its subcellular localization. Furthermore, they indicate that the presence of the NTD in the CDKL5-726X and CDKL5-781X mutants, which can still undergo condensation, can critically increase the LLPS propensity of the $CTD_{298–725}$ and CTD $_{298–780}$ fragments of the CTD, which do not appear to form condensates as such.

Finally, we tested how the aberrant LLPS of disease-related mutants may impact the functional activity of the CDKL5 kinase in the cellular context. Indeed, by altering the supramolecular organization of the protein, and/or by deleting CTD regions potentially involved in regulatory contacts with the kinase domain, C-terminal deletions may modulate the catalytic activity of the NTD. Toward this aim, we assessed the phosphorylation level of EB2, a known target of CDKL5 (Baltussen et al, 2018), in cells expressing either full-length CDKL5 or its two truncated mutants (Fig 10), using previously developed approaches (Silvestre et al, 2024).

As a preliminary step, we initially evaluated the ability of exogenously expressed WT CDKL5-GFP to enhance EB2 phosphorylation in HEK293 cells. In immunocytochemistry (ICC) experiments, we found that the relative proportion of phosphorylated EB2 was significantly enhanced in cells expressing CDKL5-GFP in comparison with control cells expressing GFP alone (Fig 10A), as detected using a phospho-specific antibody recognizing the protein only when phosphorylated at S222 ("pEB2") and an antibody recognizing the EB2 protein as such (Silvestre et al, 2024). The same result was obtained using a Western blot (WB) analysis of the levels of pEB2 versus total EB2 in lysates of HEK293 cell cultures expressing either CDKL5-GFP or GFP alone (Fig 10B). Thus, we used these approaches to quantitatively compare the catalytic activity of the two disease-related truncated mutants of CDKL5 (CDKL5-S726X and CDKL5-R781X) with that of WT CDKL5 in the cellular context (Fig 10C–F).

The ICC analysis showed that in cultured cells expressing either one of the two CDKL5 disease-related mutants, EB2 phosphorylation was significantly reduced in comparison with cells expressing WT CDKL5 (Fig 10C). A one-way ANOVA indicated overall significant differences between the experimental groups ($F_{(3,460)}$ = 135.24, P < 0.0001), and pairwise post hoc comparisons indicated significant differences between the WT CDKL5 group and both the CDKL5-S726X and CDKL5-R781X groups (n = 87–195 cells per group, P < 0.0001, NK test in both instances; Fig 10D). These results were corroborated by a WB analysis of EB2 phosphorylation in lysates of cell cultures expressing either WT, or mutant CDKL5, or GFP alone as a control (Fig 10E). Indeed, a one-way ANOVA indicated an overall significant difference across groups ($F_{(3,12)}$ = 22.556, P < 0.001), and specifically between the WT CDKL5 group and both the mutant CDKL5-S726X and CDKL5-R781X groups (n = 4 per group, P < 0.02, NK test in both instances; Fig 10F).

These findings indicate that the aberrant LLPS of CDKL5 is also associated with an impaired functional activity of the kinase in the cellular context. Specifically, our results indicate that the C-terminal portion of the protein, distal to a.a. 725, is crucial to ensure the physiological level of CDKL5 catalytic activity. This conclusion is also consistent with recent findings that missense mutations in the very distal part of the protein (T958R) can significantly alter its catalytic activity (Frasca et al, 2022).

Together with our previous observations, these findings show that the most C-terminal portion of CDKL5 (~300 residues), by means of LLPS, has key functional roles in regulating both the subcellular localization of the protein and its functional activity. As this region can be removed by distal disease-related truncating mutations, its loss––through the impairment of CDKL5 LLPS and functional activity––may play a role in the molecular pathogenesis of CDD.

Discussion

The results of our experiments reveal the intrinsic ability of CDKL5 to form condensates through LLPS and identify its serine-rich CTD, and an internal fragment of it (CTIF) together with the C-terminal tail of the protein, as key players in this process. Distal truncations, deleting the CTIF and the downstream tail of the CTD, significantly impair both LLPS and the catalytic activity of CDKL5 in the cellular context. These findings uncover the role of LLPS in the functional biology of CDKL5 and suggest a potential role of

photoactivated (triggered condensation) and fixed at 2 or 30 min after photoactivation. Statistically significant (*asterisks*) and nonsignificant (*n.s.*) differences are highlighted. The control group (mCh-Cry2) is the same as in Fig 6F as the experiments were performed in parallel.
Source data are available for this figure.

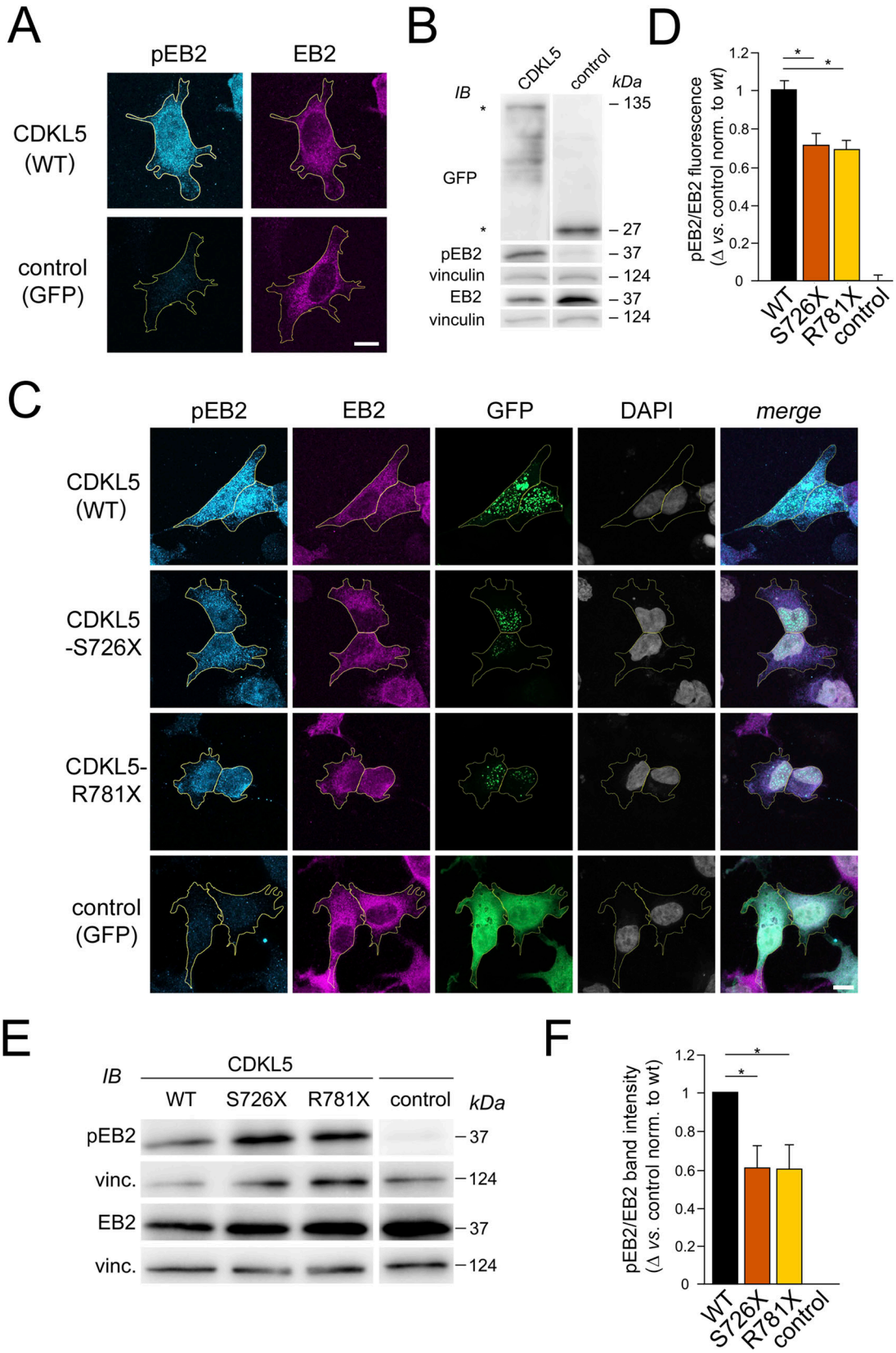

Figure 10. Mutations truncating the CDKL5 protein within the CTIF impair its catalytic activity.
(A) Representative confocal fluorescence images of HEK293 cells expressing either CDKL5-GFP (*upper row*) or GFP alone (*lower row*) and immunostained to reveal the presence of EB2 (*right column, purple*) or its S222 phosphorylated form (pEB2; *left column, cyan*). Calibration bar: 10 μm. Note the strong increase of the pEB2 signal in

aberrant LLPS in the molecular pathogenesis of CDD forms associated with distal truncations of the CTD.

Our morphological and functional experiments concurrently show that the intracellular foci formed by the CDKL5 protein display hallmark features of LLPS-driven condensates, including a rounded morphology, the ability to rapidly coalesce into larger droplets, a dynamic molecular exchange with the surrounding cellular environment, as revealed by FRAP, and the sensitivity to 1,6-Hex, which is known to disrupt the relatively weak molecular interactions underlying LLPS (Ulianov et al, 2021; Vaglietti et al, 2023). Moreover, optogenetic approaches and live-cell confocal imaging analyses, using the optoDroplet system (Shin et al, 2017), further confirmed the ability of the protein CTD, and of the CTIF within it, to condensate in a rapid and reversible manner, another characteristic feature of LLPS-prone protein regions (Basu et al, 2020; Vaglietti et al, 2023).

Spontaneous and triggered condensation assays concurrently identified the CTD, and the CTIF, as key drivers of the phase separation process. The CTD alone did not display the condensation pattern of full-length CDKL5, thus indicating that the interplay between the CTD and the NTD defines the overall LLPS behavior of the entire protein. Indeed, the NTD was able to undergo a low degree of spontaneous condensation, consistent with recent observations that a catalytic domain of another protein kinase can form LLPS-driven condensates (Qiu et al, 2024).

Molecular dissection experiments also highlighted the role of the most distal portion of the CTD, downstream of the CTIF, in promoting LLPS. Indeed, the $CTD_{726–960}$ fragment, which contains only about one third of the CTIF together with the tail of the protein, displays considerable LLPS propensity in optoDroplet assays, suggesting that the whole-region downstream residue 657 is the key CDKL5 driving region. Consistent with this conclusion, the upstream CTD fragment ($CTD_{298–725}$) did not display significant LLPS propensity in the same assays.

Two lines of evidence strongly suggest that the CTD drives LLPS autonomously and is not a client of other proteins forming condensates to which the CTD would be then secondarily recruited. First, in the optoDroplet experiments (Fig 6E–G), the CTD fused to mCh-Cry2 rapidly undergoes LLPS when photoactivated. Such photoactivation directly affects only the CTD-mCh-Cry2 protein (through the Cry2 fragment) but not other potential LLPS-driving proteins. If CTD condensation relied on the LLPS of another cellular protein, the process should not be triggered by photoactivation and the CTD-mCh-Cry2 would be recruited to condensates of other proteins even in the absence of photoactivation. Second, in optoDroplet experiments, the condensation and decondensation dynamics of photoactivated CTIF-mCh-Cry2 (Fig 7F and G) follow kinetics that are typical of a protein condensing autonomously. Indeed, CTIF condensation peaks, as typical in these experiments, 1–2 min after photoactivation and declines relatively rapidly within 10–15 min. If CTIF-mCh-Cry2 condensation was mediated by the recruitment to preexisting condensates formed by other proteins, the decondensation kinetics would not be so closely related to the timing of the photoactivating pulse.

Considering both the availability of established methodologies and criteria that we used to assess protein LLPS in the intracellular context, and growing evidence questioning the relevance of in vitro LLPS assays performed with purified proteins under highly artificial conditions (e.g., Patel et al, 2022; Poudyal et al, 2023; Hedtfeld et al, 2024; Holehouse & Alberti, 2025), we have conducted the study of CDKL5 LLPS pathophysiology in the relevant cellular context rather than in vitro.

Remarkably, the CTD and the CTIF contain a considerably high percentage (17.6% and 18%, respectively) of serine residues (8.01% on average in the human proteome). Serine-rich regions and polyserine (polyS) repeats have been implicated in protein oligo-/polymerization, interactions, LLPS, and aggregation (Pelassa & Fiumara, 2015; Lilliu et al, 2018; Sabari et al, 2018; Marchetti et al, 2021; Zhang et al, 2022; Peng et al, 2026), playing functional and evolutionary roles in biological entities ranging from viruses to multicellular organisms (Seifert et al, 2006; Yagi et al, 2014; Kim et al, 2016; Pelassa et al, 2019; Marchetti et al, 2021).

Our evolutionary analyses indicate that the long serine-rich CTD in CDKL5 is phylogenetically ancient, as it is found even in species from older taxa along the vertebrate lineage (e.g., Agnatha). The serine richness of the CTD increased further in younger clades, reaching its highest level in metatherian and eutherian mammals, suggesting its functional relevance.

Based on sequence similarity, the vertebrate CDKL paralogs are split into two groups, one comprising CDKL1-4 and the other CDKL5 alone (Canning et al, 2018). We found that the CDKL1–4 CTDs, which are considerably shorter than the CDKL5 CTD, are less

cells expressing CDKL5-GFP. **(B)** Representative Western blot of lysates of HEK293 cells expressing either CDKL5-GFP (*left lane*) or GFP alone (*right lane*) to detect the levels of these two exogenous proteins (α-GFP immunoblotting, IB) and the endogenous CDKL5 target protein EB2, as such (α-EB2 IB) or phosphorylated at Ser222 (α-pEB2 IB). Vinculin, a housekeeping protein, was used as a lane loading control (α-vinculin IB). Note how EB2 is considerably more phosphorylated in CDKL5-GFP–expressing cells in comparison with what was observed in GFP-expressing cells. Together with the results shown in panel (A), these findings indicate that the exogenously expressed GFP-tagged kinase is catalytically active and dramatically enhances EB2 phosphorylation in HEK293 cells. **(C)** As in panel (A), for cells expressing (*green* signal) either WT CDKL5, its two indicated disease-related mutants, or GFP alone (control). The cells were immunostained to reveal EB2 (in *purple*) and pEB2 (in *cyan*). Nuclei are stained using DAPI (in *gray*). Images displaying the four merged channels for each construct are shown on the right (*merge*). Scale bar: 10 μm. **(D)** Bar graph displaying the quantification of the relative proportion of phosphorylated EB2 in the experiments shown in panel (C). Columns report for each group the mean ratio between the pEB2 and EB2 fluorescent intensities in each cell, expressed as variation (Δ) versus the GFP control group and normalized to the WT CDKL5-GFP group. *Asterisks* indicate statistically significant differences. Note how the relative phosphorylation level of EB2 is significantly lower in cells expressing the two truncated kinases than in cells expressing the full-length CDKL5-GFP kinase. **(E)** As in panel (B), for lysates of cells expressing either CDKL5-GFP, or one of the indicated GFP-tagged disease-related mutants, or GFP alone as a control. Immunoblotting was performed for each experimental group using α-pEB2 and α-EB2, α-GFP, and α-vinculin (vinc) antibodies. Vinculin was used as a lane loading control. **(F)** Bar graph displaying the optical density analysis of Western blotting experiments as shown in panel (E). The columns report the ratio of the vinculin-normalized band intensities for pEB2 and EB2, expressed as variation (Δ) versus the GFP control group, normalized to the WT CDKL5-GFP group in each experiment. *Asterisks* indicate statistically significant differences. Note how, after normalization to the expression level of the housekeeping protein, the relative phosphorylation level of EB2 is lower in cells expressing the two truncated kinases than in cells expressing the full-length CDKL5-GFP kinase.
Source data are available for this figure.

enriched, or not enriched at all, in serine residues, displaying reduced or negligible predicted LLPS propensity. This suggests the possibility that an ancestral vertebrate CDKL5 protein may have contained a short CTD with some degree of serine enrichment and modest LLPS propensity. It is conceivable that in the evolution of vertebrates, these two features were then greatly enhanced in CDKL5 and either maintained at a low level or entirely lost in its paralogs. These scenarios are consistent with the view that LCRs, including amino acid repeats (AARs), contribute to the functional diversification of paralog proteins and tend to be evolutionarily maintained if functionally relevant (Persi et al, 2016, 2023; Vaglietti et al, 2025).

CDKL genes have also been found in invertebrates. *C. elegans* and *D. melanogaster* possess only a single *CDKL* gene, more closely related to the vertebrate CDKL1-4 group, bearing a short CTD. Interestingly, the CDKL5 CTDs in both these two invertebrate species contain LCRs enriched in either A/Q (*D. melanogaster*) or N/S (*C. elegans*) residues, displaying some predicted LLPS propensity, in a configuration similar to that found in human CDKL4. These findings further support the notion that the presence of LLPS-prone LCRs may represent an ancient feature of *CDKL* genes that became particularly prominent in CDKL5. The compositionally distinct LCRs found in vertebrate and invertebrate CDKL CTDs (i.e., S-rich, A/Q-rich, and N/S-rich) may derive from an ancestral LCR by divergent evolution or may have appeared independently in different clades by convergent evolution. Both these scenarios have been previously described for LCRs/AARs (Persi et al, 2016, 2023; Pelassa et al, 2019; Vaglietti & Fiumara, 2021; Vaglietti et al, 2023, 2025).

Taken together, these evolutionary analyses strongly suggest that the peculiar compositional features of the CDKL5 CTD have been preserved and further enhanced throughout phylogenesis owing to their functional role, consistent with the growing evidence supporting the functionality of LCRs, including serine-rich/polyS sequences, in proteins. Indeed, LCRs/AARs can mediate protein–protein interactions, oligo-/polymerization, LLPS, and aggregation (Fiumara et al, 2010; Pelassa et al, 2014; Pelassa & Fiumara, 2015; Vaglietti & Fiumara, 2021; Vaglietti et al, 2023). Emerging evidence from our and other laboratories shows that polyS and serine-rich LCRs can drive protein LLPS and aggregation in physiological and pathological contexts (Lilliu et al, 2018; Sabari et al, 2018; Peng et al, 2026).

Consistent with these views, the results of our experiments directly implicate the serine-rich CTD, and its most distal portions, in the LLPS-driven condensation of CDKL5 as well as in the functional regulation of the protein catalytic activity. In principle, the serine-rich CTD may be functional in driving not only the condensation of CDKL5 alone but also its cocondensation with other proteins into functional compartments (Ma et al, 2021; Vaglietti et al, 2023). Cocondensation with other proteins may underlie the recruitment of CDKL5 to subcellular compartments held together by LLPS-dependent mechanisms, such as the pre- and postsynaptic specializations, in which CDKL5 plays important physiological roles (Pizzo et al, 2016; Gurgone et al, 2023; Kontaxi et al, 2023). A few other protein kinases have been shown to undergo LLPS (López-Palacios & Andersen, 2023), indicating that condensation may represent a general physiological mechanism for the transient compartmentalization of kinase activity to specific subcellular domains. Remarkably, serine-rich and polyS sequences are present in the LCRs of the prion-like CPEB2 and CPEB3 proteins (Vaglietti et al, 2025) and other functional prions with roles in memory-related synaptic plasticity and protein-based inheritance in yeast (Si et al, 2003a, 2003b; Theis et al, 2003; Crow et al, 2008; Fiumara et al, 2010, 2015; Tsvetkov et al, 2020). As these sequences can mediate LLPS-driven protein condensation (Sabari et al, 2018) and fibrillization (Lilliu et al, 2018), they may in principle promote the formation of more persistent forms of prion-like aggregates. The biophysical properties of serine, and its "dual personality" (Uversky, 2015), may explain why this amino acid, which is polar and disorder-promoting, can also drive the formation of supramolecular assemblies with different degrees of organization, ranging from the LLPS-driven condensates observed for some proteins (Sabari et al, 2018) and CDKL5 in this study, to fibrillary aggregates when polyS repeats are found in the context of coiled-coil structures (Lilliu et al, 2018). Future studies may explore whether the serine-rich CTD mediates not only LLPS but also prion-like structural and functional switches of CDKL5 that may perpetuate its local activity within more persistent protein assemblies.

Overall, our results implicate the evolutionarily conserved serine-rich CTD—and its most distal portions in particular—in both the physiological LLPS-driven condensation of CDKL5 and the functional regulation of its catalytic activity.

The results of our experiments on the effect of distal CTD truncations on CDKL5 LLPS and function may open new perspectives to our understanding of the molecular pathogenesis of CDD. Indeed, as indicated by different studies on CDKL5 (Paulsen et al, 2006; Bahi-Buisson et al, 2008; Feng et al, 2025) and systematic screens (Torene et al, 2024), transcripts bearing pathogenic PTCs in the initial and distal parts of transcripts may escape NMD, giving rise to variably truncated protein products. Although, to our knowledge, no systematic study of NMD efficiency for transcripts bearing PTCs along the CDKL5 ORF has been performed, existing evidence indicates that transcripts encoding C-terminally truncated forms of CDKL5 can escape NMD (Bahi-Buisson et al, 2008; Feng et al, 2025).

Remarkably, the C-terminally truncated forms of CDKL5 encoded by NMD-escaping transcripts would lack variable portions of the most LLPS-prone region of the CTD comprising the CTIF and the downstream tail of the protein. Our experiments, focusing on truncations that delete one or two thirds of the CTIF together with the protein tail, show that the loss of these distal regions can cause a significant reduction in the CDKL5 condensation capacity. In agreement with this conclusion, the two deleted protein fragments ($CTD_{726–960}$ and $CTD_{781–960}$) underwent rapid phototriggered LLPS in optoDroplet assays, whereas the corresponding complementary portions of the CTD ($CTD_{298–725}$ and $CTD_{298–780}$) did not. The fact that the two latter fragments undergo some condensation when fused to the NTD, as in the CDKL5-S726X and CDKL5-S781X mutants, underscores the role of the catalytic domain of the protein in facilitating the LLPS of the CTD and its fragments.

Moreover, the CDKL5-S726X and CDKL5-S781X mutants displayed a significantly reduced catalytic activity on the known CDKL5 target protein EB2 in the cellular context. Such reduction may be the

result of the mislocalization of C-terminally truncated CDKL5, secondary to alterations in LLPS, and of the loss of possible regulatory influences of the CTD tail on the catalytic activity of the NTD. The latter hypothesis of a regulatory role of the C-terminal tail of the protein on the catalytic activity of the NTD is consistent with recent findings by Frasca et al (2022) about a novel hypermorphic missense mutation (T958R) which changes the third last amino acid of CDKL5 and enhances the catalytic activity of the protein. The deletion of the C-terminal LLPS-driving region of the CTD did not abolish CDKL5 catalytic activity but only led to its down-regulation. Such an effect, combined with the altered subcellular localization, may substantially impact the physiological function of the protein. Thus, by altering LLPS, truncations deleting the CTIF and the more distal portion of the protein significantly impair both CDKL5 localization and catalytic activity. In principle, the expression of truncated forms of CDKL5 undergoing aberrant LLPS may potentially trigger both loss-of-function and gain-of-function disease mechanisms.

CDD was initially considered a variant form of Rett syndrome (RTT) and both disorders, although distinct, share phenotypic and clinical similarities (Cutri-French et al, 2020). RTT is caused by mutations in the gene encoding the MeCP2 protein (Amir et al, 1999). Remarkably, MeCP2 has been shown to undergo LLPS and disease-related mutations of the *MECP2* gene significantly alter this process (Fan et al, 2020; Wang et al, 2020; Jiang et al, 2021). Thus, our findings that CDKL5 forms LLPS-driven condensates, and that this ability is impaired by disease-related distal truncating mutations, establish a striking parallel at the molecular level between RTT and CDD.

LLPS and its disease-related dysregulation may therefore represent key mechanisms underlying the function and dysfunction of two fundamental molecular players in closely related diseases. Indeed, LLPS dysregulation may constitute a shared mechanism between forms of CDD associated with the expression of distally truncated CDKL5 and forms of RTT associated with mutations altering MeCP2 phase separation behavior (Fan et al, 2020; Wang et al, 2020). Ultimately, these findings open new perspectives on the possible role of protein LLPS in CDD and related neurodevelopmental disorders.

Materials and Methods

Bioinformatics

The primary sequences of the five paralogous proteins of the human CDKL family (CDKL1-5) were derived from the UniProt database (available at www.uniprot.org; IDs: Q00532, Q92772, Q8IVW4, Q5MAI5, O76039). These sequences were aligned using the Cobalt multiple sequence alignment tool (NCBI; available at https://www.ncbi.nlm.nih.gov/tools/cobalt/), and the degree of sequence conservation along the alignment was plotted (Fig 1D). The primary sequences of CDKL5 orthologous proteins from 331 vertebrate species belonging to major vertebrate clades (Primates, Dermoptera, Scandentia, Glires, Laurasiatheria, Atlantogenata [i.e., Afrotheria + Xenarthra], Metatheria, Prototheria, Sauropsida, Amphibia, Actinopterygii, Chondrichthyes) and taxa (Agnatha; Fig 2A) were obtained from NCBI (available at https://www.ncbi.nlm.nih.gov/protein/) and UniProt databases. The list of protein IDs is reported in Table S1. The UniProt sequence IDs of the *D. melanogaster* and *C. elegans* CDKL proteins are Q9VMN3 and Q9U2H1, respectively. The phylogenetic tree of the species/clades of interest and clade stem ages, derived from their divergence times (million years ago, mya) with Primatomorpha (i.e., Scandentia, 85; Glires, 87; Laurasiatheria, 94; Atlantogenata, 99; Metatheria, 160; Prototheria, 180; Sauropsida, 319; Amphibia, 352; Actinopterygii, 429; Chondrichthyes, 462; Agnatha (*P. marinus*), 563 mya), were obtained from TimeTree (Kumar et al, 2017; www.timetree.org). The two sister clades within Primatomorpha (Primates and Dermoptera) were assigned a stem age corresponding to their divergence time (79 mya). Phylogenetic trees in Newick format were processed using MegaX (Kumar et al, 2018).

Amino acid frequencies in human CDKL paralogous and orthologous proteins, as well as their mean values across all proteins of the UniProt reference human proteome, were calculated as in Marchetti et al (2021) and Vaglietti et al (2025). The CAST algorithm (Promponas et al, 2000) on the PlaToLoCo web server (Jarnot et al, 2020) was used to identify low-complexity regions in CDKL5, as shown in Fig 1A. IUPred3 (Erdős et al, 2021; available at https://iupred3.elte.hu) was used to calculate a per-residue structural disorder score ("long disorder" default score) along the CDKL5 primary sequence. Thin bar graphs displaying the position of amino acids along protein primary sequences were generated using Excel. FuzDrop (Hardenberg et al, 2020) was used to calculate the overall LLPS propensity score (p_{LLPS}) of proteins of interest and to obtain per-residue LLPS propensity scores (P_{DP}) along protein primary sequences. The analyzed disease-related CDKL5 variants (see Fig 8A) were derived from the ClinVar database (available at https://www.ncbi.nlm.nih.gov/clinvar/). These variants (related to the *Homo sapiens* cyclin-dependent kinase-like 5 [CDKL5], transcript variant III, mRNA; NCBI Reference Sequence: NM_001323289.2), affecting the coding part of the gene, included nontruncating (missense and in-frame indels) and truncating (nonsense and frameshift) mutations annotated as "pathogenic" (Table S2). The atomic-level structural model of human CDKL5 was generated using AlphaFold2 (AF2; Mirdita et al, 2022; available at https://alphafold.ebi.ac.uk/) based on the primary sequences (UniProt ID: O76039; model AF-O76039-F1-model_v4 retrieved on 22 March 2023). The model was downloaded in PDB format and processed using UCSF Chimera software (version 1.14; Meng et al, 2006; see Supplemental Data 1, Supplemental Data 2, and Supplemental Data 3). The available experimental structure of the kinase domain was derived from the Protein Data Bank (PDB; available at https://www.rcsb.org) database (4bgq; Canning et al, 2018) in PDB format. These protein structures were visualized, processed, and pseudo-colored based on the FuzDrop per-residue P_{DP} score, or were used to identify specific residues, using UCSF Chimera. The potential pathogenicity of single amino acid substitutions along the primary sequence of human CDKL5 was determined based on AlphaMissense predictions (Cheng et al, 2023). The AlphaMissense plots shown in Fig 8B were either (*upper plot*) derived from the AlphaFold protein structure database (available at https://alphafold.ebi.ac.uk/entry/O76039) or (*lower plot*)

generated using Excel (Microsoft) using the per-residue "mean AM score from all" as derived from the AlphaMissense website (available at https://alphamissense.hegelab.org/hotspot). The per-residue Shannon entropy in an alignment of six CDKL5 orthologs of interest (primary sequence IDs listed above in relation to the AF2 models) generated using MultAlin (Corpet, 1988) was obtained from the Entropy-One tool available on the Los Alamos National Laboratory website (https://www.hiv.lanl.gov/content/sequence/ENTROPY/entropy_one.html). The entropy graph in Fig 8B reports only the values related to the 960 positions of the alignment corresponding to the positions of the human residues.

Plasmids and molecular cloning

Plasmid vectors for the expression of GFP- or mCh-Cry2-tagged proteins/peptides of interest were generated using the In-Fusion cloning system (Clontech-Takara). DNA fragments encoding CDKL5 or its fragments of interest were amplified by PCR from the pCAGIG vector containing the CDKL5 ORF (a kind gift of Dr. Alessandro Morellato, Molecular Biotechnology Center, University of Turin). The PCR products or interest were then subcloned into the pAcGFP-N1-In-Fusion-Ready plasmid (Clontech-Takara) or into the pX-mCh-Cry2 plasmid (Vaglietti et al, 2023).

In all cloning procedures, PCR products were obtained using the CloneAmp-HiFi PCR Premix (Clontech-Takara). The PCR primer oligonucleotides were designed with 15/18-bp extensions suitable for the In-Fusion cloning system. A Kozak sequence fragment (CACC) was also included in the forward primer immediately upstream of the CDKL5 ATG start codon. An ATG start codon was also added after the CACC Kozak sequence for the expression of internal fragments of CDKL5.

PCR products were separated by agarose gel electrophoresis and purified from agarose gels using the NucleoSpin kit (Macherey-Nagel). Purified PCR products were subcloned into linearized plasmid vectors of interest using the In-Fusion cloning system following the manufacturer's protocol. Plasmids were amplified using Stellar chemically competent cells (Clontech-Takara) and purified using the NucleoSpin plasmid Mini kit (Macherey-Nagel) or the NucleoBond Xtra MIDI EF kit (Macherey-Nagel). For all the plasmids that were generated, the protein-coding sequences were verified by Sanger sequencing.

Using this general approach, we generated plasmids for the expression of GFP-tagged CDKL5, its fragments of interest, that is, the NTD (a.a. 1–297) and the CTD (a.a. 278–960), two C-terminally truncated disease-related mutants, that is, CDKL5-S726X (a.a. 1–725) and CDKL5-R781X (a.a. 1–780), and an internal deletion mutant (CDKL5-ΔCTIF), lacking a.a. 657–840. The latter mutant was obtained through a multi-fragment In-Fusion cloning reaction with two PCR products of the ORF fragments, encoding a.a. 1–656 and a.a. 841–960, that were fused together at one of their ends and then to the vector.

To generate suitable plasmid vectors for optoDroplet induction experiments (Shin et al, 2017), the nucleotide sequences encoding CDKL5 fragments of interest, that is, the NTD, the CTD, CTD fragments (a.a. 298–725, a.a. 726–960, a.a. 298–780, a.a. 781–960), and the internal CTIF fragment (a.a. 657–840), were PCR-amplified from the pAcGFP-N1-CDKL5 plasmid using the CloneAmp-HiFi PCR Premix with primers bearing suitable 15-bp extensions to allow their subcloning into the pX-mCh-Cry2 plasmid (Vaglietti et al, 2023) using the In-Fusion cloning system. These vectors allowed the expression of the CDKL5 fragments of interest as fusion proteins with mCherry (mCh), for fluorescence visualization, and a fragment of the cryptochrome 2 protein of *A. thaliana* (Cry2), which can trigger the condensation of LLPS-prone peptides in a blue light–dependent manner (Shin et al, 2017).

For the CDKL5-GFP construct, we used the Fw1 (5′-AAGGCCTCT GTCGACCACCATGAAGATTCCTAACATTGGTAATGTG-3′) and Rv1 (5′-AGA ATTCGCAAGCTTCAAGGCTGTCTCTTTTAAATCATTCAG-3′) primers.

For the NTD-GFP construct, we used the Fw1 and Rv2 (5′-AGAATT CGCAAGCTTAAATGTAGGGTGATTCAAACACTGTTC-3′) primers. For the CTD-GFP construct, we used the Fw2 (5′-AAGGCCTCTGTCGACCACCAT GCAAACCCAGAGACTTCTGGATCGTTCT-3′) and Rv1 primers.

For the CDKL5-ΔCTIF-GFP construct, we used two pairs of primers, that is, Fw1 with Rv3 (5′-CTCTGGAGGGAGCTGTTCTCCAGGCTG GGG-3′), and Fw3 (5′-CAGCTCCCTCCAGAGAAGTTGTTACATCTCTCTTCG GCCTCAAAT-3′) with Rv1.

For the CDKL5-S726X-GFP and CDKL5-R781X-GFP constructs, we used the Fw1 primer with either the Rv4 (5′-AGAATTCGCAAGCTTATT GTCTGGACGTGGAGATGGCACTCT-3′) or the Rv5 (5′-AGAATTCGCAAG CTTGAAAAATCCTTGCTTCTCTTTTTCCTTGAG-3′) primer, respectively.

For the NTD-mCh-Cry2 construct, we used the FwA (5′-GGACTC AGATCTCGACACCATGAAGATTCCTAACATTGGTAATGTG-3′) and the RvA (5′-GAAGCTTGAGCTCGAAAATGTAGGGTGATTCAAACACTGTTC-3′) primers.

For the CTD-mCh-Cry2 construct, we used the FwB (5′-GGACTC AGATCTCGACACCATGCAAACCCAGAGACTTCTGGATCGTTCT-3′) and the RvB (5′-GAAGCTTGAGCTCGACAAGGCTGTCTCTTTTAAATCATTCAG-3′) primers.

For the CTD-298-725-mCh-Cry2 construct, we used the FwB and the RvC (5′-GAAGCTTGAGCTCGAATTGTCTGGACGTGGAGATGGCACTCT-3′) primers.

For the CTD-726-960-mCh-Cry2 construct, we used the FwC (5′-GGACTCAGATCTCGACACCATGTCTTTCCATGAAAATAATGTGTCAACT-3′) and the RvB primers.

For the CTD-298-780-mCh-Cry2 construct, we used the FwB and the RvD (5′-GAAGCTTGAGCTCGAGAAAAATCCTTGCTTCTCTTTTTCCTT GAG-3′) primers.

For the CTD-781-960-mCh-Cry2 construct, we used the FwD (5′-GGACTCAGATCTCGACACCATGAGGTCAATGAAAAAGAAAAAGAAGAAATC T-3′) and the RvB primers.

For the CTIF-mCh-Cry2 construct, we used the FwE (5′-GGACTC AGATCTCGACACCATGACTGTGGCAAGATCTTCGGTCAAAGAG-3′) and the RvE (5′-GAAGCTTGAGCTCGAGCGCAGTGACTTTAATGGCTGGCTTTGGGT-3′) primers.

Cell culture and neuronal differentiation

NG108-15 cells (Nelson et al, 1976; Christian et al, 1978; Han et al, 1991) were maintained in DMEM (Sigma-Aldrich) with 10% FBS (Sigma-Aldrich) and 1X HAT supplement (Thermo Fisher Scientific), 2 mM L-glutamine (Sigma-Aldrich), 100 units/ml penicillin (Sigma-Aldrich), and 100 μg/ml streptomycin (Sigma-Aldrich), as in Mitchell et al (2007) in an atmosphere with 5% CO_2 at 37°C. To induce neuronal differentiation, NG1081-15 cells were plated onto poly-D-lysine–coated glass coverslips (0.1 mg/ml; Sigma-Aldrich)

in 24-well plates, and after 24–48 h, the culture medium was replaced with a differentiation medium consisting of DMEM with 1% FBS, 1X HAT, 1 mM dibutyryl-cAMP (dbcAMP; Sigma-Aldrich), 2 mM L-glutamine (Sigma-Aldrich), 100 units/ml penicillin (Sigma-Aldrich), and 100 μg/ml streptomycin (Sigma-Aldrich), for 7–14 d (Mitchell et al, 2007). Half of the differentiation medium in the culture wells was replaced on alternate days. HEK293 cells (293-F strain; Thermo Fisher Scientific) were maintained following standard procedures in DMEM (Thermo Fisher Scientific) supplemented with 10% FBS, 2 mM L-glutamine (Sigma-Aldrich), 100 units/ml penicillin (Sigma-Aldrich), and 100 μg/ml streptomycin (Sigma-Aldrich) in an atmosphere with 5% CO_2 at 37°C. The cells that were used for immunocytochemistry or plasmid transfection were plated onto glass coverslips coated with poly-L-lysine (0.1 mg/ml; Sigma-Aldrich) in 24-well plates. For optoDroplet experiments, HEK293 cells were plated into 50-mm plastic culture dishes with a central 14-mm glass coverslip (MatTek) coated with poly-L-lysine.

Hippocampal cell cultures were prepared from P18 embryos (400–800 cells/mm^2) from either WT or CDKL5 knockout (KO) mice (Gurgone et al, 2023), as in Russo et al (2019). Immunocytochemistry experiments on hippocampal neurons were performed on DIV13–15. All procedures involving mice were conducted in accordance with European Community Council Directive 2010/63/EU for care and use of experimental animals with protocols approved by the Italian Minister for Scientific Research (authorization number 802/2024-PR, protocol 5CEED.166) and the Bioethics Committee of the University of Torino, Italy.

Cell culture transfection

Transfections of NG108-15 and HEK293 cells were performed 24 h after plating using Lipofectamine 2000 (Thermo Fisher Scientific) following the manufacturer's protocol, using 0.25–1 μg of plasmid DNA for each coverslip in a single well of a 24-well plate with a 3:1 Lipofectamine (μl)-to-DNA (μg) ratio. HEK293 cultures in 24-well plates transfected with the highest amount of plasmid (1 μg) for the expression of CDKL5 GFP displayed a ~12-fold increase in CDKL5 expression in comparison with the endogenous expression level (Fig S5B), in the range of similar overexpression-based studies (e.g., Burstein et al, 2018). When transfecting NG108-15 cells, the culture medium containing the transfection mix was replaced 4 h after transfection with fresh medium. Twenty-four hours after transfection, the culture medium was replaced with the differentiation culture medium and NG108-15 cells were allowed to differentiate for 7–14 d before fixation. For optoDroplet experiments, the transfection of HEK293 cells was performed on non-adherent cells in suspension, immediately before plating, using the same reagents (Vaglietti et al, 2023). The cells were then plated onto poly-L-lysine–coated coverslips. HEK293 cells were fixed at 24, 48, or 72 h after transfection. Both NG108-15 and HEK293 cells were fixed, after rinsing with PBS (3x), using 4% PFA in PBS (pH 7.4) for 15–20 min at room temperature (RT). After rinsing in PBS (3x), the coverslips were mounted onto microscope slides using Dako mounting medium (Agilent).

Immunocytochemistry (ICC)

Hippocampal, NG108-15, and HEK293 cells growing on glass coverslips were fixed in 4% PFA after rinsing with PBS (3x). The cells were then permeabilized using 0.1% Triton X-100 in PBS, pH 7.4, for 15 min, rinsed in PBS (3x), and then incubated for 1 h in blocking solution (1% BSA [Thermo Fisher Scientific] in PBS). The cells were then incubated with primary antibodies against human CDKL5 (sc-376314, dilution 1:500 in 0.1% BSA in PBS; Santa Cruz Biotechnology) for 3 h at RT. After rinsing with PBS (3x), the cells were incubated with an Alexa Fluor 488–conjugated secondary antibody (cat. #A-11001, dilution 1:1,000; Thermo Fisher Scientific) for 1 h at RT and rinsed with PBS (3x). Finally, nuclei were stained with 300 nM DAPI (Thermo Fisher Scientific) in PBS for 5 min at RT. In some experiments, filamentous actin was stained using the Phalloidin CruzFluor 555 conjugate (sc-363794; Santa Cruz Biotechnology) for 90 min at RT and rinsed in PBS (3x). The coverslips were then mounted onto microscope slides using Dako mounting medium (Agilent).

For the quantification of CDKL5-related EB2 phosphorylation in the cellular context, HEK293 cells were cultured onto poly-L-lysine–coated glass coverslips and transfected, as described above, to alternatively express either CDKL5-GFP, CDKL5-726X-GFP, CDKL5-781X-GFP, or GFP alone as a control. The expression levels of the GFP-tagged mutant forms of CDKL5 in expressing cells were similar and not statistically different from the expression level of CDKL5-GFP (Fig S5C). Forty-eight hours after transfection, the cells were fixed and processed for ICC. Briefly, HEK293 cells growing on glass coverslips were fixed in 4% PFA for 15 min. After rinsing with PBS (3x), the cells were processed using 0.5% Triton X-100, 10% normal donkey serum (NDS) in PBS, pH 7.4. The cells were then rinsed with PBS (3x) and subsequently incubated with primary antibodies, that is, α-EB2 (cat. #ab45767, 1:500 dilution; Abcam) and α-phospho-EB2 (at S222, cat. #00117741, 1:500 dilution; Covalab) in PBS containing 3% NDS and 0.5% Triton X-100 for 3 h at RT. After rinsing with PBS (3x), the cells were incubated with secondary fluorescent antibodies (Jackson ImmunoResearch, anti-rabbit [cat. #711-175-152] or anti-rat [cat. #712-165-153]; 1:1,000 dilution) in PBS containing 3% NDS and 0.5% Triton X-100 for 1 h at RT and rinsed with PBS (3x). Finally, nuclei were stained with DAPI (Thermo Fisher Scientific) in PBS, and after rinsing with PBS, the coverslips were mounted on microscopy slides with Dako mounting medium (Agilent). Multichannel confocal fluorescence images were acquired to identify GFP-positive and GFP-negative cells and measure the EB2, pEB2, and GFP ICC fluorescence signals for each cell. The individual cellular profiles were manually traced using ImageJ, and within each profile, the intensity of the pEB2, total EB2, and GFP signals was quantified using ImageJ. For each one of the three signals, we measured the mean pixel intensity over the cell area on Z-projections of the confocal image stacks obtained using the ImageJ "average intensity" algorithm. For each coverslip, we calculated the ratio between the mean pixel intensity signals for pEB2 and EB2 in both GFP-positive cells and neighboring GFP-negative control cells. The cells were considered as GFP-negative or GFP-positive, respectively, when the mean intensity of the GFP signal was lesser than 5 or greater than 10 on a 0–255 intensity scale (eight-bit images). The pEB2/EB2 signal intensity ratio of the

GFP-positive cells was normalized to the mean ratio measured in the GFP-negative control cells. For each construct, we analyzed in this manner four coverslips derived from independent replicates of the experiment (87–195 GFP-positive cells and 16–103 GFP-negative cells per coverslip). In each one of the four replicates, we measured for each cell the absolute difference (Δ) between the pEB2/EB2 ratio value and the mean value of the same ratio across the cells of the GFP control group. This Δ versus the GFP control group calculated for each cell was then normalized to the mean value of the pEB2/EB2 ratio across the cells of the CDKL5-GFP group. Using this approach, we were able to compare the relative ability of CDKL5-GFP and its disease-related mutant forms to increase EB2 phosphorylation above the basal level of phosphorylation observed in control cells.

Confocal and super-resolution (Airyscan) fluorescence microscopy

Confocal and super-resolution imaging (Airyscan) of hippocampal, NG108-15, and HEK293 cells expressing fluorescently labeled proteins of interest, or stained otherwise with secondary fluorescent antibodies, fluorescent phalloidin, and/or DAPI, was performed using a ZEISS LSM 800 Airyscan microscope (Zeiss; equipped with 405-, 488-, 561-, and 640-nm lasers) with a 63X (NA: 1.4, oil immersion) objective using default Airyscan super-resolution settings, or with a 40X (NA: 1.3, oil immersion) objective. Some confocal images were acquired using a FluoView FV300 confocal microscope (Olympus, equipped with 488- and 543-nm lasers; bearing 40X [NA:1, oil immersion] and 60X [NA: 1.4, oil immersion] objectives) or a Mica Microhub imaging platform (Leica Microsystems, equipped with 365-, 470-, 555-, and 625-nm excitation sources; 63X [NA: 1.4, oil immersion] objective) and Thunder deconvolution using the LASX software platform (Leica Microsystems). Image analysis was performed using FIJI/ImageJ (Schindelin et al, 2012).

LLPS analysis

The spontaneous formation of condensates by GFP-tagged CDKL5, its fragments, and its disease-related mutants was quantified in confocal fluorescence images of HEK293 and NG108-15 cells acquired at 24–72 h after transfection. *Z*-stack maximum intensity projections of fluorescence confocal images of 233 × 233 μm, or 350 × 350 μm, microscopy fields were converted into eight-bit images using FIJI/ImageJ (NIH). For each image, brightness and contrast were adjusted alternately to highlight either the fluorescent condensates alone or the entire profiles of fluorescent nuclei/cells. These two adjusted images were used to automatically quantify, for each image, the area and number of individual condensates, the total area occupied by condensates, and the total area of fluorescent cells/nuclei using ad hoc CellProfiler (Carpenter et al, 2006) pipelines. Condensates were detected using a combination of fluorescence intensity, which is characteristically higher than that of the surrounding nucleoplasm/cytoplasm, and size thresholds with automatic detection and counting using the CellProfiler software, as in Vaglietti et al (2023). This approach allowed to detect the typical brighter fluorescent foci while excluding occasional large areas of high-intensity signal in cells with particularly high expression levels. From these parameters, we calculated for each image the proportion of the total cell/nucleus fluorescent area occupied by condensates and the mean size of each condensate. For each experimental group, we analyzed 10–40 microscopy fields from cell cultures derived from at least three independent biological replicates of the same experiment.

To quantify rapid LLPS induction, and its kinetics, using the optoDroplet system (Shin et al, 2017), HEK293 cells, grown onto poly-L-lysine–coated glass coverslips and expressing for 24–48 h either CDKL5 fragments of interest fused to mCh-Cry2, or mCh-Cry2 alone, were photoactivated using 488-nm blue light emitted by a LED light array within a custom-made apparatus, with a working distance of 10 cm between the LEDs and the cell culture, for 4–5 min (Vaglietti et al, 2023). In pilot experiments, the blue light intensity was set at a level that triggered the condensation of an LLPS-prone mutant form of mCh-Cry2 (mCh-Cry2Olig, used as a positive control) but not of mCh-Cry2 (Shin et al, 2017). Two minutes after photoactivation, the cells were rinsed in PBS and fixed with 4% PFA in PBS. After rinsing in PBS (3x), coverslips were mounted onto microscope slides for subsequent fluorescent confocal imaging to detect the mCherry red fluorescence. Control cells were treated in the same manner, except that photoactivation was omitted. LLPS-driven condensate formation was quantified, as described above, by calculating, for each construct and treatment, the relative proportion of the mCh-positive cell area occupied by condensates using an ad hoc CellProfiler pipeline.

Live-cell imaging

Short-term live-cell optoDroplet imaging experiments of HEK293 cells expressing CTIF-mCh-Cry2 were performed using a FluoView FV300 confocal microscope (Olympus). For these experiments, the culture medium was replaced with Hanks' balanced saline solution (HBSS) and cells were incubated in a custom-made on-stage incubator for temperature control (37°C; Ragazzini et al, 2019). To highlight the coalescence of CDKL5-GFP condensates, cell cultures were imaged every 10 s. To study the condensation kinetics of the CDKL5 CTIF fragment using the optoDroplet system (see above), HEK293 cells expressing CTIF-mCh-Cry2 were imaged 30 s before and 10 min after (one image every 30 s) a photoactivating pulse was delivered using the 488-nm laser light (as in Vaglietti et al [2023]). Images were further analyzed using FIJI software and CellProfiler, as described above.

For longer (1–2 h) live-cell time-lapse imaging experiments to study condensate dynamics, HEK293 cells were plated in 10-well glass-bottom CELLview microslides (Greiner Bio-One) for 24 h and then transfected with plasmids encoding mCherry, as a whole-cell marker, and CDKL5-GFP. Imaging, using a MICA Microhub system (Leica), started 48 h post-transfection and continued for 1–2 h (one frame every 2.5 min) at 37°C in a 5% CO_2 atmosphere using an on-stage incubator (OkoLab). Cell illumination was adjusted to prevent phototoxicity in repeated scans. The image series were processed using Thunder deconvolution (Leica) and adjusted for brightness and contrast to highlight fluorescent condensates.

1,6-Hexanediol (1,6-Hex) treatments

To define the sensitivity to 1,6-Hex of intracellular condensates formed by endogenous CDKL5, HEK293 cultures were exposed to a final concentration of 5% 1,6-Hex in culture medium for 5 or 15 min (Ulianov et al, 2021; Vaglietti et al, 2023). The cells were then rinsed with PBS (3x) and fixed in 4% PFA in PBS (15–20 min at RT) and processed for ICC using a primary anti-CDKL5 antibody (sc-376314; Santa Cruz Biotechnology; see above). The treatment with 1,6-Hex was omitted in control cultures. The proportion of the fluorescent cell area occupied by condensates was measured as described above. The same protocol was also used to quantify the sensitivity to 1,6-Hex of condensates formed by exogenously expressed CDKL5-GFP at 24–48 h after transfection.

Fluorescence recovery after photobleaching (FRAP)

To perform FRAP experiments, HEK293 cells were plated at low density in eight-well glass-bottom microslides (Ibidi) and transfected to express CDKL5-GFP. FRAP experiments were performed 24–48 h after transfection, on a TCS SP8 confocal microscope (Leica) equipped with an HCX PL APO 63X/1.4 oil objective, an adaptive focus control, and stage incubator (Oko-Lab) to maintain temperature at 37°C in a 5% CO_2 atmosphere. Each individual cell nucleus was imaged for five iterations (5X zoom, pinhole 5AU), and then, a CDKL5-GFP condensate contained within a 3-μm^2 circular region of interest (ROI) was bleached using high (100%) laser power at 488 nm (Argon laser at 70% initial power, one iteration). After bleaching, images were taken every 1.625 s to monitor fluorescence recovery. For each condensate that was studied, fluorescence intensities measured before and after photobleaching were quantified for the photobleached region of interest or "ROI" (ROI1), a second ROI encompassing the entire cell (ROI2), and a third ROI encompassing the nonfluorescent background region (ROI3) using the LASX software (Leica). The data were analyzed using the easyFRAP tool (Koulouras et al, 2018) by subtracting background fluorescence (as detected in ROI3) and compensating for imaging-related fluorescence decay (as detected in ROI2). The final FRAP curve was obtained from easyFRAP using double normalization and was fitted to a double exponential curve to calculate the mobile fraction (*Mf*) and the recovery half-time ($t_{1/2}$).

Correlative light and electron microscopy (CLEM)

HEK293 cells, plated onto 35-mm dishes containing a gridded glass coverslip (MatTek) and expressing CDKL5-GFP for 24–48 h, were fixed with 4% PFA, 1% glutaraldehyde in 0.1 M Hepes buffer (pH 7.4). To obtain additional reference points for the precise alignment of the fluorescence and EM images, cell cultures expressing CDKL5-GFP were also stained with MitoTracker Red CMXRos (200 nM, Thermo Fisher Scientific) and Hoechst 33342 (Thermo Fisher Scientific) to label mitochondria and cell nuclei, respectively. Confocal images of cells expressing CDKL5-GFP were acquired using a FluoView 3000 RS system (Evident Scientific) equipped with a UPLSAPO 60X/1.3 silicon objective. Z-stacks encompassing the entire cell were acquired with an optical section depth of 0.21 μm, and the images were deconvolved using Huygens Software (SVI) before alignment with corresponding EM images. The cell cultures were postfixed with reduced osmium (1% OsO4, 1.5% potassium ferrocyanide in 0.1 M cacodylate buffer, pH 7.4) for 1 h on ice. After multiple washes in ultrapure water, they were incubated in 0.5% uranyl acetate overnight at 4°C. Samples were then dehydrated with increasing ethanol concentrations, embedded in epoxy resin, and polymerized for 48 h at 60°C. Ultrathin serial sections (70 nm thick) were obtained using a UC7 ultramicrotome (Leica), collected on formvar/carbon-coated copper slot grids, stained with uranyl acetate and Sato's lead solutions, and observed under a Talos L120C transmission electron microscope (Thermo Fisher Scientific) operating at 120 kV. Images were acquired using a Ceta CCD camera (Thermo Fisher Scientific) and aligned with confocal images using the Fiji macro-plugin Big Warp.

Cell culture lysate preparation

HEK293 cell cultures expressing either CDKL5-GFP, CDKL5-S726X-GFP, CDKL5-R781X-GFP, or GFP alone for 24 h were lysed using an ice-cold lysis buffer (150 mm NaCl, 50 mm TrisF, 5% glycerol, 1% NP-40, 1 mM $MgCl_2$) supplemented with 200 mM sodium orthovanadate, 100 mM dithiothreitol (DTT), 100 mM phenylmethylsulfonyl fluoride (PMSF), 1 M sodium fluoride, and protease inhibitors (SIGMAFAST protease inhibitor cocktail tablets, EDTA-free). The lysates were centrifuged at 13,000*g* for 10 min at 4°C to remove cell debris, and the supernatants were stored at −80°C until used for Western blot experiments. Sample protein concentrations were determined using a NanoDrop spectrophotometer (Thermo Fisher Scientific).

Dot immunoblotting

HEK293 cells transfected to alternatively express CDKL5-GFP, CDKL5-S726X-GFP, CDKL5-R781X-GFP for 72 h, as well as non-transfected control cells, were lysed as in Gurgone et al (2023) and centrifuged at 16,000*g* for 20 min at 4°C. After centrifugation, 0.5–1 μl of the supernatants was dot-immunoblotted on nitrocellulose membranes. The same volume of each sample was blotted onto two membranes, one used for GFP immunostaining, and the other for housekeeping protein staining (vinculin; see below). The membranes were allowed to air-dry for ~10 min at RT, and blocked in 2.5% nonfat dry milk in Tris-buffered saline with 0.1% Tween-20 (TBS-T) for 1 h at RT with gentle agitation. After blocking, the membranes were washed three times for 10 min with TBS-T with gentle shaking and then incubated overnight at 4°C with a primary antibody raised against GFP (cat. #pabg1-100; 1:1,000; ChromoTek) or vinculin (cat. #sc73614; 1:1,000; Santa Cruz Biotechnology), in blocking solution (2.5% milk in TBS-T). The membranes were washed three times with TBS-T (10 min per wash) and then incubated for 1 h at RT with horseradish peroxydase (HRP)-conjugated secondary antibodies, either anti-rabbit IgG (cat. #31460; 1:3,000; Thermo Fisher Scientific) or anti-mouse IgG (cat. #31430; 1:3,000; Thermo Fisher Scientific), in blocking solution. After incubation, the membrane underwent three additional 10-min washes with TBS-T. Membrane-bound secondary antibodies were detected using Enhanced

Chemiluminescence (ECL) reagent (Promega), and images were captured using the ChemiDoc imaging system (Bio-Rad).

Western blotting

Western blotting experiments have been performed as in Gurgone et al (2023). Briefly, cell lysates of HEK293 cells transfected to express either CDKL5-GFP, CDKL5-S726X-GFP, CDKL5-R781X-GFP, or GFP alone, obtained 48 h after transfection, were boiled in SDS sample buffer and separated by SDS–PAGE, and the proteins were then blotted to a PVDF membrane following standard procedures. Next, PVDF membranes were blocked in 5% nonfat dry milk in TBS with 0.1% Tween-20 for 1 h at RT and incubated with primary antibodies overnight at 4°C. We used primary antibodies directed against vinculin (cat. #AB-81457, 1:1,000 dilution; ImmunologicalSciences), EB2 (cat. #ab45767, 1:1,000 dilution; Abcam), phosphorylated EB2 (at serine 222, cat. #00117741, 1:1,000 dilution; Covalab), and GFP (cat. #pabg1-100, 1:1,000 dilution; ChromoTek). After rinsing in 0.1% Tween-20 in TBS, the membranes were incubated with the appropriate anti-rat or anti-rabbit secondary antibodies conjugated with HRP (1:5,000 dilution; Sigma-Aldrich) for 1 h at RT. The chemiluminescence signal was visualized using the Clarity Western ECL Blotting Substrate (Bio-Rad), acquired with a ChemiDoc imager (Bio-Rad), and analyzed using ImageJ software (NIH). Band intensity values related to anti-pEB2 and anti-EB2 antibodies were normalized, in each lane, to the intensity of the respective vinculin band. As detailed in the Results section, the vinculin-normalized intensity of the band obtained with the phosphospecific anti-EB2 antibody was further normalized to the vinculin-normalized intensity of the band obtained with the non–phospho-specific anti-EB2 antibody. In each one of the four independent replicates of the experiment, we measured for each experimental group the absolute difference (Δ) between the pEB2/EB2 ratio value and the mean value of the same ratio in the GFP control group. This Δ versus the GFP control group calculated for each group was then normalized to the mean value of the pEB2/EB2 ratio in the CDKL5-GFP group. Using this approach, we were able to compare the relative ability of CDKL5-GFP and its disease-related mutant forms to increase EB2 phosphorylation above the basal level observed in control cultures.

Statistics

Data and statistical analyses were performed using Excel (Microsoft) and Statistica (TIBCO) software. Data are expressed as the mean ± SEM. *t* test, ANOVA (one- or two-way) followed by post hoc tests, and Fisher's exact test were performed, when appropriate, to assess statistical significance. A P-value < 0.05 was considered statistically significant in all instances.

Data Availability

Data are available from the corresponding authors upon reasonable request.

Supplementary Information

Supplementary Information is available at https://doi.org/10.26508/lsa.202503402.

Acknowledgements

This research was supported by RiLo2022/2023 grants from the University of Turin to F Fiumara. This work was also supported by Department of Excellence funding from the Ministry of University and Research (MUR) for 2023-2027, awarded to the Department of Neurosciences "Rita Levi Montalcini" (University of Turin), and by a contribution from the Italian parent association "Albero di Greta Onlus" to M Giustetto. A previous version of this manuscript (Dell'Oca et al, 2024 *Preprint*).

Author Contributions

S Boggio Bozzo: data curation, formal analysis, validation, investigation, visualization, and writing—review and editing.
M Dell'Oca: data curation, formal analysis, investigation, visualization, and writing—review and editing.
S Vaglietti: data curation, formal analysis, investigation, visualization, and writing—review and editing.
A Gurgone: data curation, formal analysis, validation, investigation, visualization, and writing—review and editing.
V Cardinale: data curation, formal analysis, investigation, and writing—review and editing.
G Ragazzini: resources and writing—review and editing.
A Alessandrini: resources, methodology, and writing—review and editing.
L Colnaghi: data curation, formal analysis, investigation, methodology, and writing—review and editing.
JF Bazan: data curation, formal analysis, investigation, and writing—review and editing.
M Ghirardi: resources, data curation, formal analysis, methodology, project administration, and writing—review and editing.
M Giustetto: resources, data curation, formal analysis, supervision, methodology, project administration, and writing—original draft, review, and editing.
F Fiumara: conceptualization, resources, data curation, formal analysis, supervision, funding acquisition, investigation, visualization, methodology, project administration, and writing—original draft, review, and editing.

Conflict of Interest Statement

The authors declare that they have no conflict of interest.

References

Alberti S, Dormann D (2019) Liquid-liquid phase separation in disease. *Annu Rev Genet* 53: 171–194. doi:10.1146/annurev-genet-112618-043527

Amir RE, Van Den Veyver IB, Wan M, Tran CQ, Francke U, Zoghbi HY (1999) Rett syndrome is caused by mutations in X-linked MECP2, encoding Methyl-CpG-binding protein 2. *Nat Genet* 23: 185–188. doi:10.1038/13810

Bahi-Buisson N, Nectoux J, Rosas-Vargas H, Milh M, Boddaert N, Girard B, Cances C, Ville D, Afenjar A, Rio M, et al (2008) Key clinical features to identify girls with CDKL5 mutations. *Brain* 131: 2647–2661. doi:10.1093/brain/awn197

Baltussen LL, Negraes PD, Silvestre M, Claxton S, Moeskops M, Christodoulou E, Flynn HR, Snijders AP, Muotri AR, Ultanir SK (2018) Chemical genetic identification of CDKL5 substrates reveals its role in neuronal microtubule dynamics. *EMBO J* 37: e99763. doi:10.15252/embj.201899763

Barbiero I, Valente D, Chandola C, Magi F, Bergo A, Monteonofrio L, Tramarin M, Fazzari M, Soddu S, Landsberger N, et al (2017) CDKL5 localizes at the centrosome and midbody and is required for faithful cell division. *Sci Rep* 7: 6228. doi:10.1038/s41598-017-05875-z

Basu S, Mackowiak SD, Niskanen H, Knezevic D, Asimi V, Grosswendt S, Geertsema H, Ali S, Jerković I, Ewers H, et al (2020) Unblending of transcriptional condensates in human repeat expansion disease. *Cell* 181: 1062–1079.e30. doi:10.1016/j.cell.2020.04.018

Bertani I, Rusconi L, Bolognese F, Forlani G, Conca B, De Monte L, Badaracco G, Landsberger N, Kilstrup-Nielsen C (2006) Functional consequences of mutations in CDKL5, an X-linked gene involved in infantile spasms and mental retardation. *J Biol Chem* 281: 32048–32056. doi:10.1074/jbc.M606325200

Burstein SR, Valsecchi F, Kawamata H, Bourens M, Zeng R, Zuberi A, Milner TA, Cloonan SM, Lutz C, Barrientos A, et al (2018) In vitro and in vivo studies of the ALS-FTLD protein CHCHD10 reveal novel mitochondrial topology and protein interactions. *Hum Mol Genet* 27: 160–177. doi:10.1093/hmg/ddx397

Canning P, Park K, Gonçalves J, Li C, Howard CJ, Sharpe TD, Holt LJ, Pelletier L, Bullock AN, Leroux MR (2018) CDKL family kinases have evolved distinct structural features and ciliary function. *Cell Rep* 22: 885–894. doi:10.1016/j.celrep.2017.12.083

Carpenter AE, Jones TR, Lamprecht MR, Clarke C, Kang IH, Friman O, Guertin DA, Chang JH, Lindquist RA, Moffat J, et al (2006) CellProfiler: Image analysis software for identifying and quantifying cell phenotypes. *Genome Biol* 7: R100. doi:10.1186/gb-2006-7-10-r100

Cheng J, Novati G, Pan J, Bycroft C, Žemgulytė A, Applebaum T, Pritzel A, Wong LH, Zielinski M, Sargeant T, et al (2023) Accurate proteome-wide missense variant effect prediction with AlphaMissense. *Science* 381: eadg7492. doi:10.1126/science.adg7492

Christian CN, Nelson PG, Bullock P, Mullinax D, Nirenberg M (1978) Pharmacologic responses of cells of a neuroblastoma X glioma hybrid clone and modulation of synapses between hybrid cells and mouse myotubes. *Brain Res* 147: 261–276. doi:10.1016/0006-8993(78)90839-9

Corpet F (1988) Multiple sequence alignment with hierarchical clustering. *Nucleic Acids Res* 16: 10881–10890. doi:10.1093/nar/16.22.10881

Crow E, Du Z, Li L (2008) New insights into prion biology from the novel [SWI+] system. *Prion* 2: 141–144. doi:10.4161/pri.2.4.8069

Cutri-French C, Armstrong D, Saby J, Gorman C, Lane J, Fu C, Peters SU, Percy A, Neul JL, Marsh ED (2020) Comparison of core features in four developmental encephalopathies in the Rett natural history study. *Ann Neurol* 88: 396–406. doi:10.1002/ana.25797

Dai Z, Yang X (2024) The regulation of liquid-liquid phase separated condensates containing nucleic acids. *FEBS J* 291: 2320–2331. doi:10.1111/febs.16959

Dell'Oca M, Bozzo SB, Vaglietti S, Gurgone A, Cardinale V, Ragazzini G, Fiumara F (2024) The CDKL5 kinase undergoes liquid-liquid phase separation driven by a serine-rich C-terminal region and impaired by neurodevelopmental disease-related truncations. *BioRxiv*. doi:10.1101/2024.11.18.624084 (Preprint posted November 18, 2024).

Demarest S, Pestana-Knight EM, Olson HE, Downs J, Marsh ED, Kaufmann WE, Partridge C-A, Leonard H, Gwadry-Sridhar F, Frame KE, et al (2019) Severity assessment in CDKL5 deficiency disorder. *Pediatr Neurol* 97: 38–42. doi:10.1016/j.pediatrneurol.2019.03.017

Embree CM, Abu-Alhasan R, Singh G (2022) Features and factors that dictate if terminating ribosomes cause or counteract nonsense-mediated mRNA decay. *J Biol Chem* 298: 102592. doi:10.1016/j.jbc.2022.102592

Erdős G, Pajkos M, Dosztányi Z (2021) IUPred3: Prediction of protein disorder enhanced with unambiguous experimental annotation and visualization of evolutionary conservation. *Nucleic Acids Res* 49: W297–W303. doi:10.1093/nar/gkab408

Fan C, Zhang H, Fu L, Li Y, Du Y, Qiu Z, Lu F (2020) Rett mutations attenuate phase separation of MeCP2. *Cell Discov* 6: 38. doi:10.1038/s41421-020-0172-0

Fehr S, Leonard H, Ho G, Williams S, de Klerk N, Forbes D, Christodoulou J, Downs J (2015) There is variability in the attainment of developmental milestones in the CDKL5 disorder. *J Neurodev Disord* 7: 2. doi:10.1186/1866-1955-7-2

Feng X, Zhu ZA, Wang HT, Zhou HW, Liu JW, Shen Y, Zhang YX, Xiong ZQ (2025) A novel mouse model unveils protein deficiency in truncated CDKL5 mutations. *Neurosci Bull* 41: 805–820. doi:10.1007/s12264-024-01346-4

Fiumara F, Fioriti L, Kandel ER, Hendrickson WA (2010) Essential role of coiled coils for aggregation and activity of Q/N-rich prions and PolyQ proteins. *Cell* 143: 1121–1135. doi:10.1016/j.cell.2010.11.042

Fiumara F, Rajasethupathy P, Antonov I, Kosmidis S, Sossin WS, Kandel ER (2015) MicroRNA-22 gates long-term heterosynaptic plasticity in Aplysia through presynaptic regulation of CPEB and downstream targets. *Cell Rep* 11: 1866–1875. doi:10.1016/j.celrep.2015.05.034

Frasca A, Pavlidou E, Bizzotto M, Gao Y, Balestra D, Pinotti M, Dahl HA, Mazarakis ND, Landsberger N, Kinali M (2022) Not just loss-of-function variations: Identification of a hypermorphic variant in a patient with a CDKL5 missense substitution. *Neurol Genet* 8: e666. doi:10.1212/NXG.0000000000000666

Gurgone A, Pizzo R, Raspanti A, Chiantia G, Devi S, Comai D, Morello N, Pilotto F, Gnavi S, Lupori L, et al (2023) mGluR5 PAMs rescue cortical and behavioural defects in a mouse model of CDKL5 deficiency disorder. *Neuropsychopharmacology* 48: 877–886. doi:10.1038/s41386-022-01412-3

Han HQ, Nichols RA, Rubin MR, Bähler M, Greengard P (1991) Induction of formation of presynaptic terminals in neuroblastoma cells by synapsin IIb. *Nature* 349: 697–700. doi:10.1038/349697a0

Hardenberg M, Horvath A, Ambrus V, Fuxreiter M, Vendruscolo M (2020) Widespread occurrence of the droplet state of proteins in the human proteome. *Proc Natl Acad Sci U S A* 117: 33254–33262. doi:10.1073/pnas.2007670117

Hector RD, Dando O, Landsberger N, Kilstrup-Nielsen C, Kind PC, Bailey MES, Cobb SR (2016) Characterisation of CDKL5 transcript isoforms in human and mouse. *PLoS One* 11: e0157758. doi:10.1371/journal.pone.0157758

Hector RD, Kalscheuer VM, Hennig F, Leonard H, Downs J, Clarke A, Benke TA, Armstrong J, Pineda M, Bailey MES, et al (2017) CDKL5 variants: Improving our understanding of a rare neurologic disorder. *Neurol Genet* 3: e200. doi:10.1212/NXG.0000000000000200

Hedtfeld M, Dammers A, Koerner C, Musacchio A (2024) A validation strategy to assess the role of phase separation as a determinant of macromolecular localization. *Mol Cell* 84: 1783–1801.e7. doi:10.1016/j.molcel.2024.03.022

Holehouse AS, Alberti S (2025) Molecular determinants of condensate composition. *Mol Cell* 85: 290–308. doi:10.1016/j.molcel.2024.12.021

Jarnot P, Ziemska-Legiecka J, Dobson L, Merski M, Mier P, Andrade-Navarro MA, Hancock JM, Dosztányi Z, Paladin L, Necci M, et al (2020)

PlaToLoCo: The first web meta-server for visualization and annotation of low complexity regions in proteins. *Nucleic Acids Res* 48: W77–W84. doi:10.1093/nar/gkaa339

Jiang Y, Fu X, Zhang Y, Wang S-F, Zhu H, Wang W-K, Zhang L, Wu P, Wong CCL, Li J, et al (2021) Rett syndrome linked to defects in forming the MeCP2/Rbfox/LASR complex in mouse models. *Nat Commun* 12: 5767. doi:10.1038/s41467-021-26084-3

Katayama S, Sueyoshi N, Inazu T, Kameshita I (2020) Cyclin-dependent kinase-like 5 (CDKL5): Possible cellular signalling targets and involvement in CDKL5 deficiency disorder. *Neural Plast* 2020: 6970190. doi:10.1155/2020/6970190

Kato M (2006) A new paradigm for West syndrome based on molecular and cell biology. *Epilepsy Res* 70: S87–S95. doi:10.1016/j.eplepsyres.2006.02.008

Khanam T, Muñoz I, Weiland F, Carroll T, Morgan M, Borsos BN, Pantazi V, Slean M, Novak M, Toth R, et al (2021) CDKL5 kinase controls transcription-coupled responses to DNA damage. *EMBO J* 40: e108271. doi:10.15252/embj.2021108271

Kim AR, Ahn KB, Kim HY, Seo HS, Yun C-H, Han SH (2016) Serine-rich repeat adhesin Gordonii surface protein B is important for Streptococcus gordonii Biofilm formation. *J Endod* 42: 1767–1772. doi:10.1016/j.joen.2016.08.016

Kistler KE, Trcek T, Hurd TR, Chen R, Liang FX, Sall J, Kato M, Lehmann R (2018) Phase transitioned nuclear Oskar promotes cell division of Drosophila primordial germ cells. *Elife* 7. doi:10.7554/eLife.37949

Kontaxi C, Ivanova D, Davenport EC, Kind PC, Cousin MA (2023) Epilepsy-related CDKL5 deficiency slows synaptic vesicle endocytosis in central nerve terminals. *J Neurosci* 43: 2002–2020. doi:10.1523/JNEUROSCI.1537-22.2023

Koulouras G, Panagopoulos A, Rapsomaniki MA, Giakoumakis NN, Taraviras S, Lygerou Z (2018) EasyFRAP-web: A web-based tool for the analysis of fluorescence recovery after photobleaching data. *Nucleic Acids Res* 46: W467–W472. doi:10.1093/nar/gky508

Kumar S, Stecher G, Suleski M, Hedges SB (2017) TimeTree: A resource for timelines, timetrees, and divergence times. *Mol Biol Evol* 34: 1812–1819. doi:10.1093/molbev/msx116

Kumar S, Stecher G, Li M, Knyaz C, Tamura K (2018) MEGA X: Molecular evolutionary genetics analysis across computing platforms. *Mol Biol Evol* 35: 1547–1549. doi:10.1093/molbev/msy096

La Montanara P, Rusconi L, Locarno A, Forti L, Barbiero I, Tramarin M, Chandola C, Kilstrup-Nielsen C, Landsberger N (2015) Synaptic synthesis, dephosphorylation, and degradation: A novel paradigm for an activity-dependent neuronal control of CDKL5. *J Biol Chem* 290: 4512–4527. doi:10.1074/jbc.M114.589762

Leonard H, Downs J, Benke TA, Swanson L, Olson H, Demarest S (2022) CDKL5 deficiency disorder: Clinical features, diagnosis, and management. *Lancet Neurol* 21: 563–576. doi:10.1016/S1474-4422(22)00035-7

Lilliu E, Villeri V, Pelassa I, Cesano F, Scarano D, Fiumara F (2018) Polyserine repeats promote coiled coil-mediated fibril formation and length-dependent protein aggregation. *J Struct Biol* 204: 572–584. doi:10.1016/j.jsb.2018.09.001

Lin C, Franco B, Rosner MR (2005) CDKL5/Stk9 kinase inactivation is associated with neuronal developmental disorders. *Hum Mol Genet* 14: 3775–3786. doi:10.1093/hmg/ddi391

López-Palacios TP, Andersen JL (2023) Kinase regulation by liquid-liquid phase separation. *Trends Cell Biol* 33: 649–666. doi:10.1016/j.tcb.2022.11.009

Ma L, Gao Z, Wu J, Zhong B, Xie Y, Huang W, Lin Y (2021) Co-condensation between transcription factor and coactivator p300 modulates transcriptional bursting kinetics. *Mol Cell* 81: 1682–1697.e7. doi:10.1016/j.molcel.2021.01.031

Marchetti C, Vaglietti S, Rizzo F, Di Nardo G, Colnaghi L, Ghirardi M, Fiumara F (2021) Heptad stereotypy, S/Q layering, and remote origin of the SARS-CoV-2 fusion core. *Virus Evol* 7: veab097. doi:10.1093/ve/veab097

Meng EC, Pettersen EF, Couch GS, Huang CC, Ferrin TE (2006) Tools for integrated sequence-structure analysis with UCSF Chimera. *BMC Bioinformatics* 7: 339. doi:10.1186/1471-2105-7-339

Mirdita M, Schütze K, Moriwaki Y, Heo L, Ovchinnikov S, Steinegger M (2022) ColabFold: Making protein folding accessible to all. *Nat Methods* 19: 679–682. doi:10.1038/s41592-022-01488-1

Mitchell PJ, Hanson JC, Quets-Nguyen AT, Bergeron M, Smith RC (2007) A quantitative method for analysis of in vitro neurite outgrowth. *J Neurosci Methods* 164: 350–362. doi:10.1016/j.jneumeth.2007.04.021

Nelson P, Christian C, Nirenberg M (1976) Synapse formation between clonal neuroblastoma X glioma hybrid cells and striated muscle cells. *Proc Natl Acad Sci U S A* 73: 123–127. doi:10.1073/pnas.73.1.123

Oi A, Katayama S, Hatano N, Sugiyama Y, Kameshita I, Sueyoshi N (2017) Subcellular distribution of cyclin-dependent kinase-like 5 (CDKL5) is regulated through phosphorylation by dual specificity tyrosine-phosphorylation-regulated kinase 1A (DYRK1A). *Biochem Biophys Res Commun* 482: 239–245. doi:10.1016/j.bbrc.2016.11.048

Palou-Márquez G, Supek F (2025) Variable efficiency of nonsense-mediated mRNA decay across human tissues, tumors and individuals. *Genome Biol* 26: 316. doi:10.1186/s13059-025-03727-y

Patel CK, Singh S, Saini B, Mukherjee TK (2022) Macromolecular crowding-induced unusual liquid-liquid phase separation of human serum albumin via soft protein-protein interactions. *J Phys Chem Lett* 13: 3636–3644. doi:10.1021/acs.jpclett.2c00307

Paulsen M, Lund C, Akram Z, Winther JR, Horn N, Møller LB (2006) Evidence that translation reinitiation leads to a partially functional menkes protein containing two copper-binding sites. *Am J Hum Genet* 79: 214–229. doi:10.1086/505407

Pelassa I, Fiumara F (2015) Differential occurrence of interactions and interaction domains in proteins containing homopolymeric amino acid repeats. *Front Genet* 6: 345. doi:10.3389/fgene.2015.00345

Pelassa I, Corà D, Cesano F, Monje FJ, Montarolo PG, Fiumara F (2014) Association of polyalanine and polyglutamine coiled coils mediates expansion disease-related protein aggregation and dysfunction. *Hum Mol Genet* 23: 3402–3420. doi:10.1093/hmg/ddu049

Pelassa I, Cibelli M, Villeri V, Lilliu E, Vaglietti S, Olocco F, Ghirardi M, Montarolo PG, Corà D, Fiumara F (2019) Compound dynamics and combinatorial patterns of amino acid repeats encode a system of evolutionary and developmental markers. *Genome Biol Evol* 11: 3159–3178. doi:10.1093/gbe/evz216

Peng Q, Wang L, Long Y, Tian H, Xu X, Ren Z, Han Y, Jiang X, Wu Z, Tan S, et al (2026) SRSF9 mediates oncogenic RNA splicing of SLC37A4 via liquid-liquid phase separation to promote oral cancer progression. *J Adv Res* 79: 505–520. doi:10.1016/j.jare.2025.03.013

Persi E, Wolf YI, Koonin EV (2016) Positive and strongly relaxed purifying selection drive the evolution of repeats in proteins. *Nat Commun* 7: 13570. doi:10.1038/ncomms13570

Persi E, Wolf YI, Karamycheva S, Makarova KS, Koonin EV (2023) Compensatory relationship between low-complexity regions and gene paralogy in the evolution of prokaryotes. *Proc Natl Acad Sci U S A* 120: e2300154120. doi:10.1073/pnas.2300154120

Pizzo R, Gurgone A, Castroflorio E, Amendola E, Gross C, Sassoè-Pognetto M, Giustetto M (2016) Lack of Cdkl5 disrupts the organization of excitatory and inhibitory synapses and parvalbumin interneurons in the primary visual cortex. *Front Cell Neurosci* 10: 261. doi:10.3389/fncel.2016.00261

Pizzo R, Lamarca A, Sassoè-Pognetto M, Giustetto M (2020) Structural bases of atypical whisker responses in a mouse model of CDKL5 deficiency disorder. *Neuroscience* 445: 130–143. doi:10.1016/j.neuroscience.2019.08.033

Poudyal M, Patel K, Gadhe L, Sawner AS, Kadu P, Datta D, Mukherjee S, Ray S, Navalkar A, Maiti S, et al (2023) Intermolecular interactions underlie protein/peptide phase separation irrespective of sequence and structure at crowded milieu. *Nat Commun* 14: 6199. doi:10.1038/s41467-023-41864-9

Promponas VJ, Enright AJ, Tsoka S, Kreil DP, Leroy C, Hamodrakas S, Sander C, Ouzounis CA (2000) CAST: An iterative algorithm for the complexity analysis of sequence tracts. *Bioinformatics* 16: 915–922. doi:10.1093/bioinformatics/16.10.915

Qiu T, Kong Y, Wei G, Sun K, Wang R, Wang Y, Chen Y, Wang W, Zhang Y, Jiang C, et al (2024) CCDC6-RET fusion protein regulates Ras/MAPK signaling through the fusion- GRB2-SHC1 signal niche. *Proc Natl Acad Sci U S A* 121: e2322359121. doi:10.1073/pnas.2322359121

Ragazzini G, Mescola A, Corsi L, Alessandrini A (2019) Fabrication of a low-cost on-stage cell incubator with full automation. *J Biol Education* 53: 165–173. doi:10.1080/00219266.2018.1451772

Rebane AA, Ziltener P, LaMonica LC, Bauer AH, Zheng H, López-Montero I, Pincet F, Rothman JE, Ernst AM (2020) Liquid-liquid phase separation of the Golgi matrix protein GM130. *FEBS Lett* 594: 1132–1144. doi:10.1002/1873-3468.13715

Ricciardi S, Kilstrup-Nielsen C, Bienvenu T, Jacquette A, Landsberger N, Broccoli V (2009) CDKL5 influences RNA splicing activity by its association to the nuclear speckle molecular machinery. *Hum Mol Genet* 18: 4590–4602. doi:10.1093/hmg/ddp426

Rusconi L, Salvatoni L, Giudici L, Bertani I, Kilstrup-Nielsen C, Broccoli V, Landsberger N (2008) CDKL5 expression is modulated during neuronal development and its subcellular distribution is tightly regulated by the C-terminal tail. *J Biol Chem* 283: 30101–30111. doi:10.1074/jbc.M804613200

Russo I, Gavello D, Menna E, Vandael D, Veglia C, Morello N, Corradini I, Focchi E, Alfieri A, Angelini C, et al (2019) p140Cap regulates GABAergic synaptogenesis and development of hippocampal inhibitory circuits. *Cereb Cortex* 29: 91–105. doi:10.1093/cercor/bhx306

Sabari BR, Dall'Agnese A, Boija A, Klein IA, Coffey EL, Shrinivas K, Abraham BJ, Hannett NM, Zamudio AV, Manteiga JC, et al (2018) Coactivator condensation at super-enhancers links phase separation and gene control. *Science* 361: eaar3958. doi:10.1126/science.aar3958

Schindelin J, Arganda-Carreras I, Frise E, Kaynig V, Longair M, Pietzsch T, Preibisch S, Rueden C, Saalfeld S, Schmid B, et al (2012) Fiji: An open-source platform for biological-image analysis. *Nat Methods* 9: 676–682. doi:10.1038/nmeth.2019

Schmidt HB, Rohatgi R (2016) In vivo formation of vacuolated multi-phase compartments lacking membranes. *Cell Rep* 16: 1228–1236. doi:10.1016/j.celrep.2016.06.088

Seifert KN, Adderson EE, Whiting AA, Bohnsack JF, Crowley PJ, Brady LJ (2006) A unique serine-rich repeat protein (Srr-2) and novel surface antigen (epsilon) associated with a virulent lineage of serotype III Streptococcus agalactiae. *Microbiology (Reading)* 152: 1029–1040. doi:10.1099/mic.0.28516-0

Shin Y, Berry J, Pannucci N, Haataja MP, Toettcher JE, Brangwynne CP (2017) Spatiotemporal control of intracellular phase transitions using light-activated optoDroplets. *Cell* 168: 159–171.e14. doi:10.1016/j.cell.2016.11.054

Si K, Giustetto M, Etkin A, Hsu R, Janisiewicz AM, Miniaci MC, Kim J-H, Zhu H, Kandel ER (2003a) A neuronal isoform of CPEB regulates local protein synthesis and stabilizes synapse-specific long-term facilitation in aplysia. *Cell* 115: 893–904. doi:10.1016/s0092-8674(03)01021-3

Si K, Lindquist S, Kandel ER (2003b) A neuronal isoform of the aplysia CPEB has prion-like properties. *Cell* 115: 879–891. doi:10.1016/s0092-8674(03)01020-1

Silvestre M, Dempster K, Mihaylov SR, Claxton S, Ultanir SK (2024) Cell type-specific expression, regulation and compensation of CDKL5 activity in mouse brain. *Mol Psychiatry* 29: 1844–1856. doi:10.1038/s41380-024-02434-7

Taylor SS, Søberg K, Kobori E, Wu J, Pautz S, Herberg FW, Skålhegg BS (2022) The tails of protein kinase A. *Mol Pharmacol* 101: 219–225. doi:10.1124/molpharm.121.000315

Theis M, Si K, Kandel ER (2003) Two previously undescribed members of the mouse CPEB family of genes and their inducible expression in the principal cell layers of the hippocampus. *Proc Natl Acad Sci U S A* 100: 9602–9607. doi:10.1073/pnas.1133424100

Torene RI, Guillen Sacoto MJ, Millan F, Zhang Z, McGee S, Oetjens M, Heise E, Chong K, Sidlow R, O'Grady L, et al (2024) Systematic analysis of variants escaping nonsense-mediated decay uncovers candidate Mendelian diseases. *Am J Hum Genet* 111: 70–81. doi:10.1016/j.ajhg.2023.11.007

Trump N, McTague A, Brittain H, Papandreou A, Meyer E, Ngoh A, Palmer R, Morrogh D, Boustred C, Hurst JA, et al (2016) Improving diagnosis and broadening the phenotypes in early-onset seizure and severe developmental delay disorders through gene panel analysis. *J Med Genet* 53: 310–317. doi:10.1136/jmedgenet-2015-103263

Tsvetkov P, Eisen TJ, Heinrich SU, Brune Z, Hallacli E, Newby GA, Kayatekin C, Pincus D, Lindquist S (2020) Persistent activation of mRNA translation by transient Hsp90 inhibition. *Cell Rep* 32: 108001. doi:10.1016/j.celrep.2020.108001

Ulianov SV, Velichko AK, Magnitov MD, Luzhin AV, Golov AK, Ovsyannikova N, Kireev II, Gavrikov AS, Mishin AS, Garaev AK, et al (2021) Suppression of liquid-liquid phase separation by 1,6-hexanediol partially compromises the 3D genome organization in living cells. *Nucleic Acids Res* 49: 10524–10541. doi:10.1093/nar/gkab249

Uversky VN (2015) The intrinsic disorder alphabet. III. Dual personality of serine. *Intrinsically Disord Proteins* 3: e1027032. doi:10.1080/21690707.2015.1027032

Vaglietti S, Fiumara F (2021) PolyQ length co-evolution in neural proteins. *NAR Genom Bioinform* 3: lqab032. doi:10.1093/nargab/lqab032

Vaglietti S, Villeri V, Dell'Oca M, Marchetti C, Cesano F, Rizzo F, Miller D, LaPierre L, Pelassa I, Monje FJ, et al (2023) PolyQ length-based molecular encoding of vocalization frequency in FOXP2. *iScience* 26: 108036. doi:10.1016/j.isci.2023.108036

Vaglietti S, Boggio Bozzo S, Ghirardi M, Fiumara F (2025) Divergent evolution of low-complexity regions in the vertebrate CPEB protein family. *Front Bioinform* 5: 1491735. doi:10.3389/fbinf.2025.1491735

Van Bergen NJ, Massey S, Quigley A, Rollo B, Harris AR, Kapsa RMI, Christodoulou J (2022) CDKL5 deficiency disorder: Molecular insights and mechanisms of pathogenicity to fast-track therapeutic development. *Biochem Soc Trans* 50: 1207–1224. doi:10.1042/BST20220791

Wang L, Hu M, Zuo M-Q, Zhao J, Wu D, Huang L, Wen Y, Li Y, Chen P, Bao X, et al (2020) Rett syndrome-causing mutations compromise MeCP2-mediated liquid-liquid phase separation of chromatin. *Cell Res* 30: 393–407. doi:10.1038/s41422-020-0288-7

Yagi M, Bang G, Tougan T, Palacpac NMQ, Arisue N, Aoshi T, Matsumoto Y, Ishii KJ, Egwang TG, Druilhe P, et al (2014) Protective epitopes of the Plasmodium falciparum SERA5 malaria vaccine reside in intrinsically unstructured N-terminal repetitive sequences. *PLoS One* 9: e98460. doi:10.1371/journal.pone.0098460

Zhang Y, Fan S, Hua C, Teo ZWN, Kiang JX, Shen L, Yu H (2022) Phase separation of HRLP regulates flowering time in Arabidopsis. *Sci Adv* 8: eabn5488. doi:10.1126/sciadv.abn5488

The CDKL5 kinase undergoes liquid–liquid phase separation driven by a serine-rich C-terminal region

Stefania Boggio Bozzo, Marco Dell'Oca, Serena Vaglietti, Antonia Gurgone, Vita Cardinale, Gregorio Ragazzini, Andrea Alessandrini, Luca Colnaghi, J Fernando Bazan, Mirella Ghirardi, Maurizio GiustettoFerdinando Fiumara

Vol 9 | No 5 | e202503402
http://doi.org/10.26508/lsa.202503402